nature

https://doi.org/10.1038/s41586-025-09954-4

Accelerated Article Preview

Bulk superconductivity up to 96 K in pressurized nickelate single crystals

Received: 15 February 2025

Accepted: 21 November 2025

Accelerated Article Preview
Published online: 02 December 2025

Cite this article as: Li, F. et al. Bulk superconductivity up to 96 K in pressurized nickelate single crystals. *Nature* https://doi.org/10.1038/s41586-025-09954-4 (2025)

Feiyu Li, Zhenfang Xing, Di Peng, Jie Dou, Ning Guo, Liang Ma, Yulin Zhang, Lingzhen Wang, Jun Luo, Jie Yang, Jian Zhang, Tieyan Chang, Yu-Sheng Chen, Weizhao Cai, Jinguang Cheng, Yuzhu Wang, Yuxin Liu, Tao Luo, Naohisa Hirao, Takahiro Matsuoka, Hirokazu Kadobayashi, Zhidan Zeng, Qiang Zheng, Rui Zhou, Qiaoshi Zeng, Xutang Tao & Junjie Zhang

Bulk superconductivity up to 96 K in pressurized nickelate single crystals

Feiyu Li,[1†] Zhenfang Xing,[2†] Di Peng,[3,2*] Jie Dou,[4,5] Ning Guo,[6] Liang Ma,[4,7,8] Yulin Zhang,[1] Lingzhen Wang,[1] Jun Luo,[4] Jie Yang,[4] Jian Zhang,[1] Tieyan Chang,[9] Yu-Sheng Chen,[9] Weizhao Cai,[10,11] Jinguang Cheng,[4,5] Yuzhu Wang,[12] Yuxin Liu,[2] Tao Luo,[2] Naohisa Hirao,[13] Takahiro Matsuoka,[14] Hirokazu Kadobayashi,[13] Zhidan Zeng,[2] Qiang Zheng,[6] Rui Zhou,[4,5] Qiaoshi Zeng,[2,3*] Xutang Tao,[1*] and Junjie Zhang[1*]

[1]State Key Laboratory of Crystal Materials, Institute of Crystal Materials, Shandong University, Jinan, Shandong 250100, China

[2]Center for High Pressure Science and Technology Advanced Research, Shanghai 201203, China

[3]Shanghai Key Laboratory of Material Frontiers Research in Extreme Environments (MFree), Shanghai Advanced Research in Physical Sciences (SHARPS), Shanghai 201203, China

[4]Beijing National Laboratory for Condensed Matter Physics and Institute of Physics, Chinese Academy of Sciences, Beijing 100190, China

[5]School of Physical Sciences, University of Chinese Academy of Sciences, Beijing 100190, China

[6]CAS Key Laboratory of Standardization and Measurement for Nanotechnology, National Center for Nanoscience and Technology, Beijing 100190, China

[7]Key Laboratory of Materials Physics, Ministry of Education, School of Physics, Zhengzhou University, Zhengzhou 450001, China

[8]Institute of Quantum Materials and Physics, Henan Academy of Sciences, Zhengzhou 450046, China

[9]NSF's ChemMatCARS, The University of Chicago, Lemont, Illinois 60439, United States

[10]School of Materials and Energy, University of Electronic Science and Technology of China, Chengdu 611731, Sichuan, China

[11]Huzhou Key Laboratory of Smart and Clean Energy, Yangtze Delta Region Institute (Huzhou), University of Electronic Science and Technology of China, Huzhou 313001, China

[12]Shanghai Synchrotron Radiation Facility, Shanghai Advanced Research Institute, Chinese Academy of Sciences, Shanghai 201204, China

[13]Japan Synchrotron Radiation Research Institute, Sayo, Hyogo 679-5198, Japan

[14]NanoTerasu Promotion Division, Japan Synchrotron Radiation Research Institute (JASRI), Sendai, Miyagi 980-8572, Japan

[†]These authors contributed equally: Feiyu Li and Zhenfang Xing
[*]Correspondence to: di.peng@hpstar.ac.cn, zengqs@hpstar.ac.cn, txt@sdu.edu.cn and junjie@sdu.edu.cn

Abstract: Recently, the Ruddlesden-Popper bilayer nickelate $La_3Ni_2O_7$ has emerged as a superconductor with a transition temperature (T_c) of ~80 K above 14 GPa[1-3]. Achieving higher T_c in nickelate superconductors, along with the synthesis of reproducible high-quality single crystals without relying on high oxygen-pressure growth conditions, remains a significant challenge[4-7]. Here we report superconductivity up to 96 K under high pressure in bilayer nickelate single crystals synthesized at ambient pressure. Energy dispersive spectroscopy, single-crystal X-ray diffraction, nuclear quadrupole resonance, and scanning transmission electron microscopy evidenced high homogeneity and crystal quality of the flux-grown $La_2SmNi_2O_{7-\delta}$ single crystals. $La_2SmNi_2O_7$ exhibits clear bulk superconductivity, including zero resistivity ($T_{c,max}^{onset}$ = 92 K and $T_{c,max}^{zero}$ = 73 K at 21 GPa) and Meissner effect (T_c = 60 K at 20.6 GPa). Low-temperature high-pressure structural study indicates that both monoclinic and tetragonal structures can support superconductivity in this bilayer nickelate. Furthermore, we established a correlation between higher T_c under high pressures and larger in-plane lattice distortion at ambient conditions, corroborated by observing even higher T_c^{onset} of 96 K in $La_{1.57}Sm_{1.43}Ni_2O_{7-\delta}$. This study overcomes key limitations in nickelate superconductor crystal growth, resolves the crystal structure in the superconducting state, and demonstrates an effective pathway towards achieving higher T_c.

Main text

Recently, layered nickelates have emerged as the second class of unconventional superconductors with T_c exceeding the boiling point of liquid nitrogen, following the discovery of near 80 K superconductivity in the Ruddlesden-Popper (R-P) bilayer $La_3Ni_2O_7$ under high pressures[1-3]. To date, two structural types of nickelate superconductors have been reported: (i) Octahedral nickelates, including bilayer $La_3Ni_2O_7$[1] and $La_2PrNi_2O_7$[8], trilayer $La_4Ni_3O_{10}$[9-11] and $Pr_4Ni_3O_{10}$[12-14], and hybrid $La_2NiO_4{\cdot}La_3Ni_2O_7$[15,16], in bulk samples under high pressure[8-14,16] and in thin films at ambient pressure[17-21]; and (ii) Square-planar nickelates at ambient pressure, but only in thin films (infinite-layer $R_{1-x}A_xNiO_2$[22-28]: R=La, Pr, Nd, Sm; A=Ca, Sr, Eu; and quintuple-layer $Nd_6Ni_5O_{12}$[29]). Despite such structural diversity, the highest T_c in all known nickelate superconductors remains ~80 K (with zero-resistivity at ~ 60 K) [1,8,30], significantly lower than the record of cuprates (T_c~133 K[31] at ambient pressure and T_c~164 K[32] under high pressures). Thus, discovering nickelate superconductors with higher T_c remains a grand challenge in high-T_c superconductivity research.

Chemical pressure via cation substitution offers a promising strategy to enhance T_c. In iron-based superconductors, substituting smaller rare-earth elements increases T_c, peaking at 55 K in doped SmFeAsO[33]. Similarly, in nickelates, chemical pressure has induced an insulator-to-metal transition in square planar trilayer systems[34], demonstrating its efficacy in tuning electronic structure. However, theoretical calculations on bilayer $R_3Ni_2O_7$ (R=La-Sm) offer divergent predictions on T_c: Zhang *et al*. found that $La_3Ni_2O_7$ is already "optimal", with T_c decreasing as the radii of rare-earth ions decrease[4]; Pan *et al*. propose T_c increases from La to Sm, potentially doubling in $Sm_3Ni_2O_7$[5]. Experimentally, $R_3Ni_2O_7$ (R=La-Sm) compounds remain largely unexplored, with only $La_3Ni_2O_7$ synthesized to date[6]. In particular, $La_3Ni_2O_7$ single crystals were grown using the high oxygen pressure (pO_2) floating zone techniques[6,35]. However, current methods often suffer from various issues, including inhomogeneity[2,36,37], impurities[38-40], intergrowth[8], and oxygen vacancies[41]. These limitations hinder a clear understanding of the superconducting mechanism in this newly-discovered high-T_c superconductor[2,6,8,36-41], and underscore the urgency for alternative synthesis methods that circumvent high pO_2 conditions. Furthermore, single crystal growth of smaller rare-earth substituted $La_{3-x}R_xNi_2O_{7-\delta}$ (R=Pr-Lu) using the floating zone technique would require even higher pO_2 than that for $La_3Ni_2O_7$[35]; meanwhile, increasing pO_2 is likely to result in impurity phases such as $La_4Ni_3O_{10}$[35]. Here, we report a new method to synthesize bilayer nickelate single crystals at ambient pressure, and we focused our efforts on optimizing the growth of high-quality $La_{3-x}R_xNi_2O_{7-\delta}$ (R=Pr-Er, $x \leq 2.67$) single crystals and their superconductivity.

Single crystal growth at 1 atm

Fig. 1a shows a scheme of the growth setup via the flux method. **Fig. 1b** shows an SEM image of a typical $La_3Ni_2O_7$ single crystal. The as-grown $La_3Ni_2O_{7-\delta}$ belongs to the monoclinic $P2_1/m$ space group (**Fig. 1d** and **Extended Data Table 1**), lower than *Amam*[1]. Our finding is consistent with the theoretical calculations that $P2_1/m$ has a lower total energy compared with *Amam*[42]. A similar symmetry lowering from orthorhombic to monoclinic has been reported in $La_4Ni_3O_{10}$[35]. Nevertheless, the out-of-plane Ni-O-Ni bond angle, which is believed to be important for superconductivity[1], remains 168.5(3)º (**Fig. 1e**), the same as *Amam*[1]. Rietveld refinement on X-ray powder diffraction data verified our single crystal structural model (**Fig. 1h**). Compared with the high-pressure floating zone growth[1,38-40], our method removed the competing phase $La_2NiO_4{\cdot}La_4Ni_3O_{10}$, and significantly improve crystal quality, as evidenced by single-crystal X-ray diffraction (SXRD) and scanning transmission electron microscopy (STEM) (**Extended Data Fig. 1**) and the three-times narrower nuclear quadrupole resonance (NQR) linewidth of our single crystals than that of polycrystalline samples[8] (**Fig. 2d**). However, two issues still exist: (i)

hybrid $La_2NiO_4 \cdot La_3Ni_2O_7$[15] single crystals emerge as a secondary phase (**Fig. 1h**), and (ii) intergrowth of R-P phases is clearly seen from NQR measurements (**Fig. 2d**) [8].

We then explored if substitution can inhibit intergrowth in single crystals, inspired by Wang et al's work on $La_2PrNi_2O_7$ polycrystalline powders[8]. We started with La:R=2:1 (R=Pr-Lu) in flux growth, and black and shiny single crystals of $La_{3-x}R_xNi_2O_7$ (R=Pr-Er) were obtained (**Fig. 1c** and **Extended Data Fig. 2**). The value of x in $La_{3-x}R_xNi_2O_{7-\delta}$ (R=Pr-Er) was determined to be $x<1$ for R=Eu-Er and $x\sim1$ for R = Pr-Sm. Interestingly, a single phase was obtained for the Sm case (**Fig. 1i**). By suppressing the hybrid R-P phase (**Supplementary Fig. 1**), the dimensions of $La_2SmNi_2O_{7-\delta}$ single crystals were increased to 220 μm on the edge (**Fig. 1c**), almost twice that of $La_3Ni_2O_7$. **Fig. 1f** shows the crystal structure of $La_2SmNi_2O_{7-\delta}$, characterized by monoclinic $P2_1/m$ (**Extended Data Table 1**). Unexpectedly, Sm preferentially occupies the La site between bilayers (**Fig. 1f**). The out-of-plane Ni-O-Ni angle is 164.2(5)° (**Fig. 1g**), smaller than $La_3Ni_2O_7$. The calculated bond valence sum values of Ni are 2.67 and 2.70, similar to $La_3Ni_2O_7$ (2.67 and 2.69), indicating that the incorporation of Sm does not change the valence state of Ni. Rietveld refinement (**Fig. 1i**) converged to R_{exp} = 3.27%, R_{wp} = 7.11% and GOF = 2.18, corroborating the single crystal structural model.

Next, we move to tune the substitution level, x, for R=Pr-Sm. The maximum x for Pr, Nd, and Sm was determined to be 2.67, 2.13, and 1.43, respectively (**Extended Data Fig. 2**). Anisotropic change in lattice parameters is observed with the increase of x (**Supplementary Figs. 2a-f**). **Extended Data Table 2** summarizes the flux growth result of $La_{3-x}R_xNi_2O_{7-\delta}$ (R=La-Er). Expectedly, the maximum x decreases with the decreasing of the size of rare earth ions (**Fig. 1j**). Of significant importance is that the molar ratio of (La+R) to Ni maintains 3:2. With the decreasing of ion size, the lattice parameters (a, b and c) at the maximum substitution exhibit anisotropy and non-monotonicity (**Supplementary Figs. 2g,h**). **Fig. 1k** shows the average in-plane lattice constants for the maximum substitution (**Supplementary Fig. 3**) in $La_{3-x}R_xNi_2O_{7-\delta}$ (R=La-Er) calculated by $a_{average}=(a^2+b^2)^{1/2}/2$ along with the lattice constants in the superconducting states[1,8,17]. With the decrease of rare earth ions, $a_{average}$ shows a non-monotonic trend, reaching a minimum at R=Nd with x=2.13. Unfortunately, even the smallest $a_{average}$ is at least 1.6% larger than those in the superconducting state[1,8,17], implying that high pressure is needed to induce superconductivity.

Crystal quality

Considering the largest size of $La_2SmNi_2O_{7-\delta}$ single crystals in our growth, we evaluate their crystal quality on the average and local structure level. **Fig. 2a** shows the energy dispersive spectroscopy (EDS) mapping on a typical as-grown $La_2SmNi_2O_{7-\delta}$ single crystal with dimensions of ~200 μm on the edge. The compositions at different positions are identical, demonstrating excellent homogeneity over the range of the whole crystal. **Fig. 2b** and **Fig. 2c** show the reconstructed (0kl) and (h0l) planes of a $La_2SmNi_2O_{7-\delta}$ single crystal measured by single crystal X-ray diffraction at 296(2) K. The observed peaks are neat and obey the selection rule of $P2_1/m$, demonstrating high crystallinity on the average structure. We then employed NQR as a sensitive, global probe to investigate possible intergrowth (**Fig. 2d**). The NQR spectrum exhibits a broad resonance peak due to positional disorder at the La (2) sites, as revealed by SXRD. The lack of resonance lines at 16 and 17 MHz indicates significantly reduced intergrowth in $La_2SmNi_2O_{7-\delta}$ single crystals, similar to $La_2PrNi_2O_7$ polycrystalline samples[8]. We further investigated the local structure of $La_2SmNi_2O_{7-\delta}$ single crystals using STEM. A typical high-angle annular dark-field (HAADF)-STEM image in the projection [110] (**Fig. 2e)** shows that $La_2SmNi_2O_{7-\delta}$ single crystals have perfectly ordered bilayer alternating stacks on the scale of tens of nanometers. To verify that it is a

universal feature in such single crystals, more than twenty different regions in two single crystals were measured, all revealing perfectly ordered stacking sequences without intergrowth. The chemical distribution of La, Sm, and Ni from the EDS diagram is shown in **Fig. 2f**. These results show that Sm preferentially occupies the La site between bilayers, consistent with SXRD (**Fig. 1f**). Thus, EDS, SXRD, NQR, and STEM evidenced high homogeneity and crystallinity of our bilayer $La_2SmNi_2O_{7-\delta}$ single crystals grown from ambient flux. The chemical pressure induced by smaller rare earth ions such as Sm effectively inhibits the intergrowth of R-P phases and maintains the integrity of the bilayer structure, consistent with Wang et al. [8]

Bulk superconductivity at 92 K

Signature of superconductivity was observed in the as-grown single crystals (**Extended Data Fig. 3a**) with T_c^{onset} = 87.7 K; however, zero resistivity was not observed, probably due to oxygen defects. We then performed post annealing to reduce oxygen defects, and we found that post annealing at pO_2 = 1.5 bar for 10 days is optimal (**Extended Data Figs. 3-5, Crystals #1-5,7**). **Figs. 3a,b** show the pressure-dependent resistivity of Crystal #6 using helium as the pressure-transmitting medium (PTM). With increasing pressure, the resistivity of $La_2SmNi_2O_7$ gradually decreased and superconductivity emerged at 14.3 GPa with T_c^{onset} = 68 K and T_c^{zero} = 4 K. Upon compression to 15.5 GPa, significantly improved zero resistivity was observed (T_c^{onset} = 68 K and T_c^{zero} = 47 K). Both T_c^{onset} and T_c^{zero} increase with increasing pressure, and they reach maximum values at 21.6 GPa with $T_{c,\,max}^{onset}$ = 92 K and $T_{c,\,max}^{zero}$ = 73 K (**Fig. 3c**), which are higher than any known superconducting nickelates[1,2,8-10,12,16,18,22-28,30,36]. Beyond 21.6 GPa, both T_c^{onset} and T_c^{zero} drop upon further compression.

Fig. 3c presents the field effects on the resistivity of $La_2SmNi_2O_7$ under a pressure of 21.6 GPa. Under zero magnetic field, a sharp superconducting transition with ~10 K in width was observed. A pronounced suppression of superconductivity by applied magnetic fields was observed. Upper critical fields extracted using the normal-state resistance values at 90%, 50%, and 10% of the resistivity near T_c^{onset}, represented by open circles, are shown in **Fig. 3d**. Using the Ginzburg-Landau model to fit Hc_2(T), zero-temperature values of 210.5 T, 108.9 T, and 61.7 T were obtained. We obtained coherence lengths of 1.3 nm, 1.7 nm, and 2.3 nm, which are comparable to those of bulk $La_3Ni_2O_7$[6]. The fan-shaped broadening of the superconducting transition under a magnetic field is a typical manifestation of flux creep in high-T_c superconductors. The significant differences in the values of the upper critical field (Hc_2) defined by different criteria are a specific reflection of such behavior.

Meissner effect, another hallmark of superconductivity, was observed. **Fig. 3e** shows the direct-current magnetic susceptibility of $La_2SmNi_2O_7$ under a magnetic field of 10 Oe at 20.6 GPa. As can be seen, clear diamagnetic signals below 60 K with substantial superconducting shielding volume fractions (>60%) were detected (**Extended Data Fig. 6** and **Calculation of superconducting volume fraction** in **Methods**). The observation of similar superconducting transitions in multiple samples (**Fig. 3** and **Extended Data Fig. 3**) demonstrates high quality and excellent reproducibility of our single crystals. Before entering superconductivity, linear-in-temperature resistivity was observed in the normal state (**Extended Data Fig. 7**), which resembles that with $La_3Ni_2O_7$[2], $La_4Ni_3O_{10}$[9], and cuprates[43].

Structure in the superconducting state

Fig. 4a shows the synchrotron X-ray powder diffraction (XRPD) patterns of $La_2SmNi_2O_7$ (pulverized Crystal #8) under various pressures at room temperature. As the pressure increases, the diffraction peaks at Q~2.3 Å^{-1} and 4.0 Å^{-1} gradually merge (**Figs. 4b,c**), suggesting a structural transition occurs at ~ 18

GPa from $P2_1/m$ to $I4/mmm$. The structural transition was also observed in another sample (pulverized Crystal #9) with a nearly identical transition pressure (**Extended Data Figs. 8a-c**). Rietveld refinements were performed to extract structural parameters and **Fig. 4e** shows the fitting on data collected at 23.2 GPa. The lattice parameters of $La_2SmNi_2O_7$ under various pressures are presented in **Figs. 4f,g**. Notably, *a* and *b* axes merge at around 18 GPa. The continuous decrease in *V* upon compression indicates a weak first-order or a second-order structural transition from $P2_1/m$ to $I4/mmm$. Such a high symmetry has been previously reported in $La_3Ni_2O_7$[44], $La_2PrNi_2O_7$[8], and $La_4Ni_3O_{10}$[9] under high pressure. To resolve the crystal structure in the superconducting state, we conducted in situ high-pressure low-temperature XRPD measurements on pulverized Crystal #10 (**Fig. 4d** and **Extended Data Fig. 8d**). $La_2SmNi_2O_7$ maintains its $P2_1/m$ down to 64 K at 17.9 GPa, even as it enters the superconducting state. This observation indicates that the monoclinic phase can support superconductivity. Upon further compression to higher pressures and cooling to lower temperatures, $La_2SmNi_2O_7$ became a tetragonal phase characterized by $I4/mmm$. Thus, our low-temperature high-pressure structural study suggests that both monoclinic and tetragonal symmetry can support superconductivity in this material.

T-P phase diagram

Fig. 4h presents the phase diagram of $La_2SmNi_2O_{7-\delta}$ as a function of temperature and pressure by summarizing transport and structural data from multiple samples. The phase diagram consists of three electronic phases - normal metal, strange metal and superconductor, and two different crystal structures - $P2_1/m$ and $I4/mmm$. Three features are identified: (1) Strange-metal behavior is observed before entering the superconducting state. This phenomenon is similar to $La_3Ni_2O_7$, [2] $La_2PrNi_2O_7$, [8] and $La_4Ni_3O_{10}$[9] and cuprates[43], indicating that strange metallicity is a common feature in unconventional superconductors; (2) Both monoclinic and tetragonal structures can support superconductivity, indicating that a tetragonal structure is not a prerequisite for the emergence of superconductivity. Our result is consistent with Shi et al[45], who reported that orthorhombic $La_3Ni_2O_7$ superconducts under high pressure. (3) No metal-to-metal (MTM) transitions were found at low pressures. The absence of such a transition, which was attributed to charge density wave (CDW) in $La_3Ni_2O_7$[46-48], indicates that CDW is probably not directly related to superconductivity in $La_2SmNi_2O_{7-\delta}$. Besides CDW, a spin density wave (SDW) at ~ 150 K was reported in $La_3Ni_2O_7$[46]. Whether SDW exists in $La_2SmNi_2O_{7-\delta}$ remains elusive. Our preliminary magnetic susceptibility measurements show a weak anomaly at ~ 147 K in $La_2SmNi_2O_7$, which may correspond to SDW (**Extended Data Fig. 9**).

T_c increased to 96 K

Fig. 5a presents the $T_{c,\,max}^{onset}$ and $T_{c,\,max}^{zero}$ of bilayer $La_3Ni_2O_7$, [1,2,30,45] $La_2PrNi_2O_7$, [8] and $La_2SmNi_2O_7$ as a function of ambient-pressure in-plane lattice distortion Δ, which is an indicator of chemical pressure induced by substitution. Interestingly, both $T_{c,\,max}^{onset}$ and $T_{c,\,max}^{zero}$ increase with increasing Δ. Guided by this insight, we extracted the lattice parameters of all $La_{3-x}R_xNi_2O_{7-\delta}$ (R=La-Er) shown in **Extended Data Table 2** and calculated their Δ (**Fig. 1l**). Notably, Δ shows a dome shape as a function of rare earth elements with the largest value from $La_{0.87}Nd_{2.13}Ni_2O_{7-\delta}$ and the second largest from $La_{1.57}Sm_{1.43}Ni_2O_{7-\delta}$. We measured the resistivity of $La_{1.57}Sm_{1.43}Ni_2O_{7-\delta}$ at high pressures and found a $T_{c,\,max}^{onset}$ of 96 K at 21.6 GPa using helium as PTM (**Extended Data Fig. 10**), which is the highest T_c among all nickelate superconductors (**Fig. 5b**) [1,2,8-10,12,16,18,22-28,30,36]. This result validates our strategy for T_c enhancement.

Conclusion

Reproducible high-quality single crystals of rare-earth-substituted bilayer nickelates have been grown at ambient pressure. As an example, superconducting transition onset temperature at 92 K with zero-

resistivity up to 73 K and Meissner effect at 60 K was achieved in pressurized $La_2SmNi_2O_7$ single crystals, demonstrating bulk high-T_c superconductivity. Low-temperature high-pressure structural study suggested that both $P2_1/m$ and $I4/mmm$ can support superconductivity. Moreover, we establish that $T_{c,max}^{onset}$ of bilayer nickelates under high pressure correlates with ambient-pressure in-plane lattice distortion. Guided by this insight, we further enhanced $T_{c,max}^{onset}$ to 96 K in $La_{1.57}Sm_{1.43}Ni_2O_{7-\delta}$, which is the highest T_c reported so far among nickelate superconductors. Our work offers a new method for synthesizing reproducible high-quality bilayer nickelate single crystals at ambient pressure, resolves the crystal structure in the superconducting state, and more importantly, provides a promising pathway for further improving T_c in nickelate superconductors.

References

1 Sun, H. L. *et al.* Signatures of superconductivity near 80 K in a nickelate under high pressure. *Nature* **621**, 493-498 (2023).

2 Zhang, Y. N. *et al.* High-temperature superconductivity with zero resistance and strange-metal behaviour in $La_3Ni_2O_7$. *Nat. Phys.* **20**, 1269-1273 (2024).

3 Wen, J. Y. *et al.* Imaging the Meissner effect in pressurized bilayer nickelate with integrated multi-parameter quantum sensor. *Natl. Sci. Rev.* **12**, nwaf268 (2025).

4 Zhang, Y., Lin, L.-F., Moreo, A., Maier, T. A. & Dagotto, E. Trends in electronic structures and s±-wave pairing for the rare-earth series in bilayer nickelate superconductor $R_3Ni_2O_7$. *Phys. Rev. B* **108**, 165141 (2023).

5 Pan, Z., Lu, C., Yang, F. & Wu, C. Effect of Rare-Earth Element Substitution in Superconducting $R_3Ni_2O_7$ under Pressure. *Chin. Phys. Lett.* **41**, 087401 (2024).

6 Wang, M., Wen, H.-H., Wu, T., Yao, D.-X. & Xiang, T. Normal and superconducting properties of $La_3Ni_2O_7$. *Chin. Phys. Lett.* **41**, 077402 (2024).

7 Wang, Y. X. *et al.* Recent progress in nickelate superconductors. *Natl. Sci. Rev.* **12**, nwaf373 (2025).

8 Wang, N. N. *et al.* Bulk high-temperature superconductivity in pressurized tetragonal $La_2PrNi_2O_7$. *Nature* **634**, 579-584 (2024).

9 Zhu, Y. *et al.* Superconductivity in pressurized trilayer $La_4Ni_3O_{10-\delta}$ single crystals. *Nature* **631**, 531-536 (2024).

10 Zhang, M. *et al.* Superconductivity in Trilayer Nickelate $La_4Ni_3O_{10}$ under Pressure. *Phys. Rev. X* **15**, 021005 (2025).

11 Li, F. *et al.* Single-Crystal Structure Determination of Superconducting $La_4Ni_3O_{10-\delta}$ under High Pressure. *Adv. Mater.*, e07365 (2025).

12 Zhang, E. *et al.* Bulk Superconductivity in Pressurized Trilayer Nickelate $Pr_4Ni_3O_{10}$ Single Crystals. *Phys. Rev. X* **15**, 021008 (2025).

13 Chen, X. *et al.* Low fractional volume superconductivity in single crystals of $Pr_4Ni_3O_{10}$ under pressure. *Phys. Rev. B* **111**, 094525 (2025).

14 Pei, C. *et al.* Pressure-Induced Superconductivity in $Pr_4Ni_3O_{10}$ Single Crystals. Preprint at https://arxiv.org/abs/2411.08677 (2024).

15 Li, F. *et al.* Design and synthesis of three-dimensional hybrid Ruddlesden-Popper nickelate single crystals. *Phys. Rev. Mater.* **8**, 053401 (2024).

16 Shi, M. *et al.* Pressure induced superconductivity in hybrid Ruddlesden–Popper $La_5Ni_3O_{11}$ single crystals. *Nat. Phys.*, https://doi.org/10.1038/s41567-41025-03023-41563 (2025).

17 Ko, E. K. *et al.* Signatures of ambient pressure superconductivity in thin film $La_3Ni_2O_7$. *Nature* **638**, 935-940 (2024).

18 Zhou, G. *et al.* Ambient-pressure superconductivity onset above 40 K in $(La,Pr)_3Ni_2O_7$ films. *Nature* **640**, 641-646 (2025).

19 Liu, Y. *et al.* Superconductivity and normal-state transport in compressively strained $La_2PrNi_2O_7$ thin films. *Nat. Mater.* **24**, 1221-1227 (2025).

20 Hao, B. *et al.* Superconductivity in Sr-doped $La_3Ni_2O_7$ thin films. *Nat. Mater.* **24**, 1756-1762 (2025).

21 Zihao Nie, Y. L., Wei Lv, Lizhi Xu, Zhicheng Jiang, Peng Fu, Guangdi Zhou, Wenhua Song, Yaqi Chen, Heng Wang, Haoliang Huang, Junhao Lin, Dawei Shen, Peng Li, Qi-Kun Xue, Zhuoyu Chen. Ambient-pressure superconductivity and electronic structures of engineered hybrid nickelate films. Preprint at https://arxiv.org/abs/2509.03502 (2025).

22 Li, D. *et al.* Superconductivity in an infinite-layer nickelate. *Nature* **572**, 624-627 (2019).

23 Osada, M., Wang, B. Y., Lee, K., Li, D. & Hwang, H. Y. Phase diagram of infinite layer praseodymium nickelate $Pr_{1-x}Sr_xNiO_2$ thin films. *Phys. Rev. Mater.* **4**, 121801 (2020).

24 Osada, M. *et al.* Nickelate Superconductivity without Rare-Earth Magnetism: $(La,Sr)NiO_2$. *Adv. Mater.* **33**, 2104083 (2021).

25 Zeng, S. *et al.* Superconductivity in infinite-layer nickelate $La_{1-x}Ca_xNiO_2$ thin films. *Sci. Adv.* **8**, eabl9927 (2022).

26 Chow, S. L. E., Luo, Z. Y. & Ariando, A. Bulk superconductivity near 40 K in hole-doped $SmNiO_2$ at ambient pressure. *Nature* **642**, 58-63 (2025).

27 Sahib, H. *et al.* Superconductivity in $PrNiO_2$ Infinite-Layer Nickelates. *Adv. Mater.* **37**, 2416187 (2025).

28 Parzyck, C. T. *et al.* Superconductivity in the Parent Infinite-Layer Nickelate $NdNiO_2$. *Phys. Rev. X* **15**, 021048 (2025).

29 Pan, G. A. *et al.* Superconductivity in a quintuple-layer square-planar nickelate. *Nat. Mater.* **21**, 160-164 (2022).

30 Li, J. Y. *et al.* Identification of superconductivity in bilayer nickelate $La_3Ni_2O_7$ under high pressure up to 100 GPa. *Natl. Sci. Rev.* **12**, nwaf220 (2025).

31 Schilling, A., Cantoni, M., Guo, J. D. & Ott, H. R. Superconductivity above 130 K in the Hg–Ba–Ca–Cu–O system. *Nature* **363**, 56-58 (1993).

32 Gao, L. *et al.* Superconductivity up to 164 K in $HgBa_2Ca_{m-1}Cu_mO_{2m+2+\delta}$ (m=1, 2, and 3) under quasihydrostatic pressures. *Phys. Rev. B* **50**, 4260-4263 (1994).

33 Zhi-An, R. *et al.* Superconductivity at 55 K in Iron-Based F-Doped Layered Quaternary Compound $Sm[O_{1-x}F_x]FeAs$. *Chin. Phys. Lett.* **25**, 2215 (2008).

34 Zhang, J. *et al.* Large orbital polarization in a metallic square-planar nickelate. *Nat. Phys.* **13**, 864-869 (2017).

35 Zhang, J. *et al.* High oxygen pressure floating zone growth and crystal structure of the metallic nickelates $R_4Ni_3O_{10}$ (R=La, Pr). *Phys. Rev. Mater.* **4**, 083402 (2020).

36 Hou, J. *et al.* Emergence of High-Temperature Superconducting Phase in Pressurized $La_3Ni_2O_7$ Crystals. *Chin. Phys. Lett.* **40**, 117302 (2023).

37 Zhou, Y. *et al.* Investigations of key issues on the reproducibility of high-T_c superconductivity emerging from compressed $La_3Ni_2O_7$. *Matter Radiat. Extremes* **10**, 027801 (2025).

38 Chen, X. *et al.* Polymorphism in the Ruddlesden–Popper Nickelate $La_3Ni_2O_7$: Discovery of a Hidden Phase with Distinctive Layer Stacking. *J. Am. Chem. Soc.* **146**, 3640-3645 (2024).

39 Puphal, P. *et al.* Unconventional Crystal Structure of the High-Pressure Superconductor $La_3Ni_2O_7$. *Phys. Rev. Lett.* **133**, 146002 (2024).

40 Wang, H. Z., Chen, L., Rutherford, A., Zhou, H. D. & Xie, W. W. Long-Range Structural Order in a Hidden Phase of Ruddlesden-Popper Bilayer Nickelate $La_3Ni_2O_7$. *Inorg. Chem.* **63**, 5020-5026 (2024).

41 Dong, Z. *et al.* Visualization of oxygen vacancies and self-doped ligand holes in $La_3Ni_2O_{7-\delta}$. *Nature* **630**, 847-852 (2024).

42 Chen, X., Jiang, P., Li, J., Zhong, Z. & Lu, Y. Charge and spin instabilities in superconducting $La_3Ni_2O_7$. *Phys. Rev. B* **111**, 014515 (2025).

43 Keimer, B., Kivelson, S. A., Norman, M. R., Uchida, S. & Zaanen, J. From quantum matter to high-temperature superconductivity in copper oxides. *Nature* **518**, 179-186 (2015).

44 Wang, L. *et al.* Structure Responsible for the Superconducting State in $La_3Ni_2O_7$ at High-Pressure and Low-Temperature Conditions. *J. Am. Chem. Soc.* **146**, 7506-7514 (2024).

45 Shi, M. *et al.* Spin density wave rather than tetragonal structure is prerequisite for superconductivity in $La_3Ni_2O_{7-\delta}$. *Nat. Commun.* **16**, 9141 (2025).

46 Khasanov, R. *et al.* Pressure-enhanced splitting of density wave transitions in $La_3Ni_2O_{7-\delta}$. *Nat. Phys.* **21**, 430-436

(2025).

47 Luo, J. *et al.* Microscopic evidence of charge- and spin-density waves in $La_3Ni_2O_{7-\delta}$ revealed by ^{139}La-NQR. *Chin. Phys. Lett.* **42**, 067402 (2025).

48 Ain, N. u. *et al.* Synthesis and characterization of single crystal and polycrystalline $La_3Ni_2O_{7-\delta}$. *Curr Appl Phys* **74**, 19-24 (2025).

Main figure legends

Fig.1 | Ambient-pressure flux growth and characterization. a, Scheme of crystal growth at ambient pressure. **b,c**, Typical scanning electron microscopy (SEM) images of $La_3Ni_2O_{7-\delta}$ and $La_2SmNi_2O_{7-\delta}$ single crystals. **d**, Crystal structure of $La_3Ni_2O_{7-\delta}$. **e**, Ball-and-stick drawings of the NiO_6 octahedra of $La_3Ni_2O_{7-\delta}$ with bond distances and bond angles labeled. **f**, Crystal structure of $La_2SmNi_2O_{7-\delta}$. **g**, Ball-and-stick drawings of the NiO_6 octahedra of $La_2SmNi_2O_{7-\delta}$ with bond distances and bond angles labeled. **h,i**, Rietveld refinements on X-ray powder diffraction data of pulverized single crystals of $La_3Ni_2O_{7-\delta}$ and $La_2SmNi_2O_{7-\delta}$, respectively. **j**, Maximum substitution of La and molar ratio of (La+R):Ni for different rare earth elements in as-grown $La_{3-x}R_xNi_2O_{7-\delta}$ (R=La-Er) single crystals. **k**, The average in-plane lattice constants of $La_{3-x}R_xNi_2O_{7-\delta}$ (R=La-Er) calculated by $a_{average}=(a^2+b^2)^{1/2}/2$ compared with those in superconducting states[1,8,17]. **l**, Ambient-pressure in-plane lattice distortion $\Delta = (a-b)/(a+b)$ of bilayer nickelates $La_{3-x}R_xNi_2O_{7-\delta}$ (R=La-Er).

Fig. 2 | Crystal quality of as-grown $La_2SmNi_2O_{7-\delta}$ single crystals. a, Energy dispersive spectroscopy (EDS) mapping of a typical $La_2SmNi_2O_{7-\delta}$ single crystal. **b,c**, Reconstructed (0*kl*) and (*h*0*l*) planes from in-house X-ray single crystal diffraction data of a $La_2SmNi_2O_{7-\delta}$ single crystal collected at 296(2) K. **d**, ^{139}La (2) nuclear quadrupole resonance (NQR) spectra corresponding to the $\pm5/2 \leftrightarrow \pm7/2$ transition in $La_3Ni_2O_{7-\delta}$ and $La_2SmNi_2O_{7-\delta}$ crystals at 188 K. The solid lines represent fits using Lorentz and Gaussian functions for $La_3Ni_2O_{7-\delta}$[8] and $La_2SmNi_2O_{7-\delta}$, respectively. **e**, A typical atomic-scale HAADF-STEM image in the projection of [110] with overlaid crystal structure model of $La_2SmNi_2O_{7-\delta}$ single crystal. Note BL is short for bilayer. **f**, EDS maps from STEM for La, Sm and Ni.

Fig. 3 | Bulk high-T_c superconductivity in $La_2SmNi_2O_7$ under high pressures. **a**, Temperature-dependent resistivity of Crystal #6 (annealed at pO_2=1.5 bar for 10 days) under pressure in a helium-filled diamond anvil cell (DAC) under pressures below 14.3 GPa. **b**, Temperature-dependent resistivity of Crystal #6 under pressures from 15.5 GPa to 30.3 GPa. **c**, Field effects on the resistivity of Crystal #6 at 21.6 GPa. The upper-left and lower-right insets illustrate the temperature-dependent resistivity behavior in the vicinity of T_c^{onset} and T_c^{zero}, respectively. **d**, Upper critical fields extracted using the normal-state resistance values at 90%, 50%, and 10% of the resistivity at T_c^{onset}. Note open circles represent data and solid lines show the fit using the Ginzburg–Landau model. **e**, Direct-current (DC) magnetic susceptibility of single-crystal $La_2SmNi_2O_7$ (Crystal #11, annealed at pO_2=1.5 bar for 10 days) measured at 20.6 GPa under an applied magnetic field of 10 Oe using both zero-field-cooled (ZFC) and field-cooled (FC) modes. Note that BG is short for background.

Fig. 4 | Structure and *T-P* phase diagram of $La_2SmNi_2O_{7-\delta}$. a, Room-temperature synchrotron X-ray powder diffraction (XRD) patterns of $La_2SmNi_2O_7$ (pulverized Crystal #8, annealed at pO_2=1.5 bar for 10 days) in the *Q* range of 1.6-6 Å^{-1} (λ = 0.4834 Å) under different pressures with helium as the pressure-transmitting medium (PTM). **b**, Enlarged view of **a** in the *Q* range of 2.15-2.45 Å^{-1}. **c**, Enlarged view of **a** in the *Q* range of 3.9-4.15 Å^{-1}. **d**, Powder XRD patterns of $La_2SmNi_2O_7$ (pulverized Crystal #10, annealed at pO_2=1.5 bar for 10 days) in the *Q* range of 2.0-2.6 Å^{-1} (λ = 0.4133 Å) at various temperatures and pressures using helium as the PTM. **e**, Rietveld refinement of $La_2SmNi_2O_7$ powder XRD pattern at 23.2 GPa at 295 K using *I*4/*mmm*. The Inset illustrates the refinement in the *Q* range of 2.2-2.6 Å^{-1}. Note cyan circles, red lines, blue lines, and green bars represent observed intensities, calculated intensities, intensity difference, and peak positions, respectively. **f,g**, Extracted lattice parameters of $La_2SmNi_2O_7$ from Rietveld refinements at 295 K. Crystal #8 (C #8) and Crystal #9 (C #9, annealed at pO_2=1.5 bar for

10 days) represent two independent experiments. **h,** *T*-*P* phase diagram of $La_2SmNi_2O_{7-\delta}$. Black squares, red circles, blue triangles, green triangles, violet diamonds, khaki triangles, and wine hexagons represent the T_c^{onset} of Crystal #1 to #7 under pressure, respectively. Cyan triangles and light-green stars represent the T_c^{zero} of Crystal #6 and #7 under pressure, respectively. Red hollow circles and squares represent the $P2_1/m$ and $I4/mmm$ of pulverized Crystal #8 (C #8), respectively. Cyan hollow circles and squares represent the $P2_1/m$ and $I4/mmm$ of pulverized Crystal #9 (C #9), respectively. Blue hollow circles and squares represent the $P2_1/m$ and $I4/mmm$ of pulverized Crystal #10 (C #10, annealed at pO_2=1.5 bar for 10 days), respectively.

Fig. 5 | A strategy for T_c enhancement and record-high T_c. a, Maximum T_c of bilayer nickelates as a function of ambient-pressure in-plane lattice distortion $\Delta=(a-b)/(a+b)$. $T_{c,max}^{onset}$ and $T_{c,max}^{zero}$ of $La_3Ni_2O_7$[1,2,30,45] and $La_2PrNi_2O_7$[8] are from resistivity measurements. The blue and yellow lines are only for guiding eyes. **b,** Maximum T_c for various nickelates[1,2,8,9,12,16,22,26].

Methods

Single crystal growth. All crystal growth was carried out at ambient pressure. La_2O_3 (Sigma-Aldrich, 99.99%) was baked at 600 ℃ for 5 h before use. Rare Earth Oxide, and NiO (Alfa Aesar, 99.99%) powders were weighed, mixed and ground, and then placed in an Al_2O_3 crucible. The mixture was mixed with anhydrous K_2CO_3 powders, which were used as a flux ($La_{3-x}R_xNi_2O_7$:K_2CO_3=1:15, mass ratio). The crucible was covered with a lid in order to minimize the evaporation of K_2CO_3. Loading anhydrous K_2CO_3 was performed in a glove box. Crystal growth was achieved via flux evaporation in a period of 72 h at a temperature of 1000-1050 ℃, followed by furnace cooling to room temperature.

Powder X-ray diffraction (PXRD). A Bruker AXS D2 Phaser X-ray powder diffractometer was used to check phase purity. Data were collected at room temperature using Cu-K_α radiation (λ = 1.5418 Å) in the 2θ range of 20-90° with a scan step size of 0.02° and a scan time of 2 s per step. TOPAS 6 was used for Rietveld refinement. Refined parameters include zero shift, background (chebychev function, order 5), lattice parameters, size L and strain G.

Single-Crystal Structure Determination. Single crystal X-ray diffraction data were collected on a Bruker AXS D8 Venture (Mo-K_α radiation, λ = 0.71073 Å) diffractometer at 296 K. A single crystal of $La_3Ni_2O_{7-\delta}$ with dimensions of 0.055×0.041×0.035 mm^3 and a single crystal of $La_2SmNi_2O_{7-\delta}$ with 0.033×0.025×0.013 mm^3 were used. Indexing was performed using Bruker APEX5 software[49]. Data integration and cell refinement were performed using SAINT, and multi-scan absorption corrections were applied using the SADABS program[49]. The structure was solved by direct methods and refined with full matrix least-squares methods on F^2. All atoms were modeled using anisotropic ADPs, and the refinements converged for $I > 2\sigma(I)$, where I is the intensity of reflections and σ(I) is the standard deviation. Calculations were performed using SHELXTL[49] and Olex2[50]. Further details of the crystal structure investigations may be obtained from the joint CCDC/FIZ Karlsruhe online deposition service by quoting the deposition numbers 2315725 and 2418256. Synchrotron X-ray single-crystal diffraction data of annealed $La_2SmNi_2O_{7-\delta}$ were collected using synchrotron radiation (λ = 0.43060 Å) at GeoSoilEnviroCARS (Sector 13) at the Advanced Photon Source, Argonne National Laboratory. A single crystal with dimensions of ~10 μm was mounted to the tip of a glass fiber and measured using a Huber 3-circle diffractometer. Indexing, data reduction, and precession images were performed using Bruker APEX5 software[49].

NQR. NQR measurements were conducted using a phase-coherent pulsed NQR spectrometer. ^{139}La-NQR spectra were obtained by sweeping the frequency point by point, and integrating spin-echo intensity. The quantity of the single crystal sample used for NQR measurement is about 100 mg.

STEM. $La_3Ni_2O_{7-\delta}$ and $La_2SmNi_2O_{7-\delta}$ single crystals were crushed in ethanol, and drops of the suspensions were deposited on lacey carbon-coated copper grids and dried in air for STEM observations. High-angle annular dark-field (HAADF)-STEM images were obtained at an accelerating voltage of 300 kV on an aberration-corrected transmission electron microscope (Spectra 300, Thermo Fisher Scientific), equipped with a field-emission electron gun. The probe convergence semi-angle and inner collection semi-angle are 25.0 mrad and 49.0 mrad, respectively.

Scanning Electron Microscopy (SEM). The morphology of the as-grown crystals was examined using a scanning electron microscope. The SEM images were obtained by GeminiSEM-300 microscope with an incident electron of 15.0 kV.

EDS. The X-ray spectrometer Bruker Quantax XFlash6-100 was used for qualitative and quantitative analysis of the as-grown crystals.

In-situ high-pressure resistivity measurements. High-pressure resistivity measurements on $La_2SmNi_2O_{7-\delta}$ single crystals under pressures up to 31.5 GPa were carried out using a BeCu-type diamond anvil cell (DAC). The sample was loaded into a pre-indented gasket hole filled with helium as the pressure-transmitting medium in between a pair of diamond anvils with a 400 μm culet. Four gold leads were manually put on the sample surface, and the electrical contact was maintained by mechanical contact. The van der Pauw four-probe method and the standard four-probe technique were both utilized for resistivity measurements under high pressures. Tiny ruby balls placed near the sample in the DAC sample chamber are used as the pressure calibrant, and the pressure is determined by monitoring the position of the ruby fluorescence R1 line at room temperature. All measurements were carried out using a Physical Property Measurement System by Quantum Design. The temperature range covered was from 2 K to 310 K, and magnetic fields up to 7 T were applied.

In-situ high-pressure direct-current (DC) magnetic susceptibility measurements. Ultra-sensitive magnetic susceptibility measurements were performed under high pressure using a custom-fabricated miniature diamond anvil cell. The cell body was machined from beryllium-copper alloy and equipped with a rhenium gasket. The cell incorporates 400 μm diameter diamond anvils compressing a sample chamber 260 μm in diameter, defined by the rhenium gasket aperture. A single crystal of $La_2SmNi_2O_7$ (approximate dimensions: 180 μm in diameter and 20 μm in thickness) was loaded into the chamber alongside liquid helium, which served as the pressure-transmitting medium to establish hydrostatic conditions. Measurements were conducted utilizing a Magnetic Property Measurement System (MPMS3, Quantum Design).

In-situ high-pressure powder X-ray diffraction measurements. To ensure the sample experienced optimal hydrostatic pressure conditions, these measurements were performed using helium as the PTM, consistent with the medium employed in our electrical transport studies. Room temperature high-pressure powder X-ray diffraction (XRD) investigations were conducted on pulverized single crystals of $La_2SmNi_2O_{7-\delta}$ at the beamline 17UM of Shanghai Synchrotron Radiation Facility (SSRF). The experiment utilized a monochromatic X-ray beam (λ = 0.4834 Å) with helium as the pressure-transmitting medium. Two-dimensional diffraction patterns were acquired using an area detector (PILATUS R CdTe) and subsequently converted to one-dimensional diffraction profiles using Dioptas software[51]. Quantitative structural analysis was performed through Rietveld refinement implemented in Jana2020[52] and GSAS-II[53] software packages, allowing precise determination of lattice parameters across different pressure regimes. In situ high-pressure synchrotron XRD experiments were conducted at BL10XU[54] of Japan's SPring-8 facility, utilizing X-rays with a wavelength of 0.4133 Å. A powder sample derived from a high-quality $La_2SmNi_2O_7$ single crystal was mounted into the sample chamber of a diamond anvil cell with a 400 μm dimension. After laser-drilling a 240 μm-diameter hole into a pre-compressed rhenium gasket (50 μm thick), helium was employed as the pressure-transmitting medium. A small gold foil and ruby marker were positioned adjacent to the sample pellet to serve as internal pressure references. The DAC was installed into an in-situ cryostat system and thoroughly evacuated prior to cooling. Pressure control was achieved remotely using a helium membrane gas regulation system. At the sample position, the X-ray beam was focused to a size of approximately 8 μm. Pressure values from both the ruby and gold markers were collected prior to and following diffraction data acquisition; the sample pressure was determined as

the average of these two datasets.

TGA measurement. The oxygen content of annealed $La_2SmNi_2O_{7-\delta}$ samples was determined by calculating the mass difference before and after complete reduction in 4% H_2/Ar using a Mettler-Toledo TGA/DSC^{3+}. The sample was measured in an alumina crucible and started at 100 °C, held for 1 hour, then heated to 900 °C, held for 2 hours, and finally cooled to 100 °C, held for 1 hour. Three blanks were run previously to establish a good baseline. The resolution of our equipment is around 10 µg.

Calculation of superconducting volume fraction. The magnetic susceptibility reported in SI units was converted from Gaussian units using the relation:

$$\chi_{0-SI} = 4\pi\chi_{CGS} = \frac{4\pi M}{HV} \quad (1)$$

where M, H, and V denote magnetic moment, applied field, and sample volume, respectively. The superconducting volume fraction was determined from the difference in magnetic moment measured at 40 K and 60 K. The sample was nominally cylindrical, with a diameter d = 180 µm and thickness h = 20 µm. The raw superconducting volume fractions measured under zero-field-cooled (ZFC) and field-cooled (FC) conditions at 40 K were -1.313 and -0.164, respectively.

Geometric demagnetization effects were corrected by applying a demagnetizing factor N, calculated using Equation

$$N^{-1} \approx 1 + 1.6\frac{h}{d} \quad (2)$$

For the sample geometry, N=0.849. This factor remains pressure-independent under hydrostatic conditions due to proportional lattice contraction. The adjusted susceptibility χ_{SI} was subsequently determined via the relation

$$N = \frac{1}{\chi_{0-SI}} - \frac{1}{\chi_{SI}} \quad (3)$$

After correction, the adjusted susceptibility χ_{SI} for ZFC and FC were -0.621 and -0.144, respectively, yielding SC volume fractions of 62.1% for ZFC mode and 14.4% for FC mode.

Data availability

The data supporting the findings of this study are available from the corresponding authors upon request or at Zenodo (https://doi.org/10.5281/zenodo.17310348)[55]. The detailed crystal structure data from this study have been deposited in the Cambridge Crystallographic Data Centre (CCDC) website with the deposition numbers 2315725 and 2418256. Source data are provided with this paper.

49 Computer code APEX5, Bruker Analytical X-ray Instruments, Inc. Madison, Wisconsin, USA (2023).

50 Dolomanov, O. V., Bourhis, L. J., Gildea, R. J., Howard, J. A. K. & Puschmann, H. OLEX2: a complete structure solution, refinement and analysis program. *J. Appl. Crystallogr.* **42**, 339-341 (2009).

51 Prescher, C. & Prakapenka, V. B. DIOPTAS: a program for reduction of two-dimensional X-ray diffraction data and data exploration. *High Pressure Res.* **35**, 223-230 (2015).

52 Petříček, V., Palatinus, L., Plášil, J. & Dušek, M. Jana2020 – a new version of the crystallographic computing system Jana. *Z. Kristallogr. - Cryst. Mater.* **238**, 271-282 (2023).

53 Toby, B. H. & Von Dreele, R. B. GSAS-II: the genesis of a modern open-source all purpose crystallography software package. *J. Appl. Crystallogr.* **46**, 544-549 (2013).

54 Hirao, N. *et al.* New developments in high-pressure X-ray diffraction beamline for diamond anvil cell at SPring-8. *Matter Radiat. Extremes* **5**, 018403 (2020).

55 Li, F. *et al.*, Bulk superconductivity up to 96 K in pressurized nickelate single crystals [Data set], Zenodo, https://doi.org/10.5281/zenodo.17310348

Acknowledgements
Work at Shandong University was supported by the National Natural Science Foundation of China (Grants Nos. 12074219 and 12374457) and the TaiShan Scholar of Shandong Province (Grants Nos. tsqn201909031 and tspd20221102). This work was supported by the National Key Research and Development Projects of China (Grants Nos. 2023YFA1406103, 2024YFA1611302, 2024YFA1409200, 2023YFA1406100 and 2022YFA1403402), the National Natural Science Foundation of China (Grants Nos. 12374142, 12304170, 12025408, 12274062, 12304030 and U23A6003). Q.S.Z. and D.P. acknowledge the support from Shanghai Key Laboratory of Material Frontiers Research in Extreme Environments, China (Grant No. 22dz2260800), and the Shanghai Science and Technology Committee, China (Grant No. 22JC1410300). We thank the BL17UM (https://cstr.cn/31124.02.SSRF.BL17UM) of Shanghai Synchrotron Radiation Facility for the assistance on in-situ high-pressure XRD measurements. The synchrotron radiation experiments were performed at BL10XU of SPring-8 with the approval of the Japan Synchrotron Radiation Research Institute (JASRI) (Proposal Nos. 2025A1472). A portion of this work was carried out at the Synergetic Extreme Condition User Facility (SECUF, https://cstr.cn/31123.02.SECUF).

Author contributions
J.Z. and X.T. conceived the research project. J.Z. coordinated the experiments. F.L. grew single crystals, performed the powder and single-crystal X-ray diffraction experiments, carried out SEM, EDS, magnetic susceptibility, and transport measurements at ambient pressure with the help of L.W., Jian Z. and J.Z. Y.Z. carried out TGA measurements with the help of J.Z. T.C. and Y.-S.C. performed synchrotron X-ray single crystal diffraction. D.P. performed the resistivity using helium and paraffin as the pressure-transmitting medium under pressure with the help of Q.S.Z. D.P. and Z.F.X. performed direct-current magnetic susceptibility measurements under high pressure using helium as the pressure-transmitting medium with the help from Q.S.Z. D.P., Z.F.X., Y.Z.W., Z.D.Z., and Q.S.Z. performed synchrotron X-ray powder diffraction measurements and data analysis under high-pressure using helium as the pressure-transmitting medium. D.P., Z.F.X., Y.X.L., T.L., N.H., T.M., H.K., Z.D.Z., and Q.S.Z. performed high-pressure and low-temperature synchrotron X-ray powder diffraction measurements and data analysis. L.M., J.C. and Z.C. performed high pressure measurements using solid or liquid as the pressure-transmitting medium. N.G. and Q.Z. carried out STEM measurements. J.D., J.L., J.Y., and R.Z. performed NQR measurements. F.L., D.P., Z.F.X., J.D., L.M., L.W., W.C, J.C., Q.Z., R.Z., X.T., and J.Z. discussed and analyzed data. F.L., J.Z., D.P., and Q.S.Z. wrote the draft with contributions from all coauthors.

Competing interests
The authors declare no conflict of interest.

Additional information
Correspondence and requests for materials should be addressed to Di Peng, Qiaoshi Zeng, Xutang Tao or Junjie Zhang.
Reprints and permissions information is available at http://www.nature.com/reprints.

Extended Data Figure/Table legends

Extended Data Fig. 1 | Crystal quality of as-grown $La_3Ni_2O_{7-\delta}$ single crystals. a,b Reconstructed (0*kl*) and (*h*0*l*) planes from in-house X-ray single crystal diffraction data of $La_3Ni_2O_{7-\delta}$ single crystal collected at 296(2) K using $P2_1/m$ with $a \sim 5.45$ Å, $b \sim 5.39$ Å, $c \sim 10.62$ Å and $\beta \sim 104.8$ Å. **c**, A typical atomic-scale HAADF-STEM image in the projection of [110] with overlaid crystal structure model of $La_3Ni_2O_7$.

Extended Data Fig. 2 | SEM images and EDS measurements of $La_{3-x}R_xNi_2O_{7-\delta}$ (R=Pr-Er) single crystals.

Extended Data Fig. 3 | Electrical transport measurements of $La_2SmNi_2O_{7-\delta}$ crystals under high pressure. a, Temperature-dependent resistivity of Crystal #1 (as-grown) measured in a helium-filled diamond anvil cell (DAC) at 21.0 GPa. The upper Inset depicts the temperature-dependent resistivity around T_c^{onset}. **b**, Temperature-dependent resistivity of Crystal #2 (annealed at pO_2=2.5 bar for 10 days) measured in a helium-filled DAC at 21.4 GPa. The Inset depicts the temperature-dependent resistivity in the vicinity of T_c^{onset}. **c,d**, Temperature-dependent resistance of Crystal #3 (annealed at pO_2=1.5 bar for 10 days) measured in a paraffin-filled DAC at 22.1 GPa. The resistance of Bridge 1 and Bridge 2 represents the electrical resistance measured along two orthogonal directions separated by 90º. The observation of similar behaviors in the electrical resistance measured along two orthogonal directions evidences excellent homogeneity in the single crystal. **e**, Field dependence of resistivity of Crystal #3 at 24.6 GPa. **f**, Temperature-dependent resistivity of Crystal #4 (annealed at pO_2=1.5 bar for 10 days) measured in a helium-filled DAC at 23.7 GPa. The upper Inset presents magnetic field effects on the superconducting transition in Crystal #4. The lower Inset shows a photograph of the electrodes used for high-pressure resistivity measurements. Helium as the pressure-transmitting medium under high pressure maintained the integrity of the single-crystal sample, and direct contact was established between the sample and the gold electrodes. **g**, Temperature-dependent resistivity of Crystal #5 (annealed at pO_2=1.5 bar for 7 days) under different magnetic field at 20.9 GPa, with helium as the pressure-transmitting medium. **h**, Temperature-dependent resistivity for Crystal #5 at 20.9 GPa near T_c^{zero}. **i,** Resistivity of Crystal #7 (annealed at pO_2=1.5 bar for 10 days) measured in a helium-filled DAC at 21.2 GPa. The Inset shows zero resistivity at 73 K.

Extended Data Fig. 4 | Reconstructed (0*kl*) and (*h*0*l*) planes of $La_2SmNi_2O_7$ (annealed at pO_2=1.5 bar for 10 days) from single crystal X-ray diffraction using *Cmcm* with $a \sim 20.3$ Å, $b \sim 5.46$ Å and $c \sim 5.36$ Å at 296(2) K. Violations are clearly seen in the (0*kl*) plane with *k*=odd and in the (*h*0*l*) plane with *l*=odd. We find the crystal symmetry maintains $P2_1/m$.

Extended Data Fig. 5 | Determination of oxygen content of the $La_2SmNi_2O_{7-\delta}$ samples annealed at pO_2 = 1.5 bar for 10 days. a,**d** Analysis of the TGA data revealed essentially stoichiometry with $\delta \approx 0.00(2)$ for sample #1 and 0.02(1) for sample #2. **b**,**c** Rietveld refinement on PXRD data of sample #1 before and after TGA measurements. **e**,**f** Rietveld refinement on PXRD data of sample #2 before and after TGA measurements.

Extended Data Fig. 6 | Temperature-dependent magnetic susceptibility of $La_2SmNi_2O_7$ under high pressure. a, Direct-current (DC) magnetic susceptibility of single-crystal $La_2SmNi_2O_7$ samples measured at 22.7 GPa under an applied magnetic field of 10 Oe using both zero-field-cooled (ZFC) and field-cooled

(FC) modes. **b**, Direct-current (DC) magnetic susceptibility measured under an applied magnetic field of 15 Oe. Note SF is short for superconducting volume fraction.

Extended Data Fig. 7 | Electrical transport measurements of $La_2SmNi_2O_7$ under high pressure. a, Temperature-dependent resistivity of Crystal #6 (annealed at pO_2=1.5 bar for 10 days) under different magnetic fields at 21.6 GPa, with helium as the pressure-transmitting medium. **b**, Temperature-dependent resistivity of Crystal #6 under zero magnetic field at 21.6 GPa, with helium as the pressure-transmitting medium. The normal state in the temperature range of 100 - 200 K shows a linear temperature dependence, a characteristic of strange-metal behaviour (red line). **c**, Temperature-dependent resistivity of Crystal #7 (annealed at pO_2=1.5 bar for 10 days) under different magnetic fields at 21.2 GPa, with helium as the pressure-transmitting medium.

Extended Data Fig. 8 | Synchrotron X-ray powder diffraction patterns of $La_2SmNi_2O_7$ (pulverized Crystal #9 and #10, annealed at pO_2=1.5 bar for 10 days) under high pressure. a, Room temperature synchrotron X-ray powder diffraction patterns of $La_2SmNi_2O_7$ (Crystal #9) in the Q range of 1.6-6 $Å^{-1}$ (λ = 0.4834 Å) under different pressures at 295 K. Note blue dot line indicates diffraction peaks from Re. **b**, Enlarged view of the patterns (Crystal #9) in the Q range of 2.15-2.45 $Å^{-1}$, highlighting the gradual merging of diffraction peaks. **c**, Enlarged view of the patterns (Crystal #9) in the Q range of 3.85-4.15 $Å^{-1}$. **d.** Synchrotron X-ray powder diffraction patterns of $La_2SmNi_2O_7$ (Crystal #10) in the Q range of 1-6 $Å^{-1}$ (λ = 0.4133 Å) at various temperatures (20-270 K) and pressures (0.6-20.2 GPa) using helium as the pressure-transmitting medium. Note that blue dot line indicates diffraction peaks from Re gasket.

Extended Data Fig. 9 | Magnetic susceptibility data of pulverized $La_2SmNi_2O_7$ single crystals annealed at 1.5 bar for 10 days. Note ZFC_W indicates zero field cooling followed by data collection on warming.

Extended Data Fig. 10 | Superconductivity at 96 K in $La_{1.57}Sm_{1.43}Ni_2O_{7-\delta}$ single crystals under high pressures. a, Temperature-dependent resistance of Crystal #1 at 17 GPa. **b,** Temperature-dependent resistance of Crystal #1 (annealed at pO_2=1.5 bar for 10 days) at 24.1 GPa. The Inset shows the zoom-in region around T_c^{onset}. **c,** Temperature-dependent resistance of Crystal #1 in the range of 19.8-28.1 GPa. The pressure was lowered from 24.1 GPa in **b** to 19.8 GPa, and then increased to 28.1 GPa. Note the step-like feature at around 80 K is absent in **b**, thus it's an artifact due to the inhomogeneity of pressure environment of paraffin. **d,** A zoom-in region around T_c^{onset}= 96 K at 26.8 GPa for Crystal #1. **e**, Temperature-dependent resistance of Crystal #2 (as grown) in the pressure range of 14.0-29.6 GPa. **f**, Temperature-dependent resistance of Crystal #2 at 29.6 GPa. The Inset shows the zoom-in region around T_c^{onset}= 96 K. **g,** Temperature-dependent resistivity of Crystal #3 (annealed at pO_2=1.5 bar for 10 days) at 21.6, 24.3 and 26.5 GPa. **h,** The zoom-in region around T_c^{onset} = 96 K at 21.6 GPa. **i,** Field dependence of resistivity of Crystal #3 at 21.6 GPa. Note that zero resistivity has not yet been achieved for $La_{1.57}Sm_{1.43}Ni_2O_{7-\delta}$ probably due to oxygen defects.

Extended Data Table 1 | Crystallographic data for $La_3Ni_2O_7$ and $La_2SmNi_2O_7$ from SXRD.

Extended Data Table 2 | Summary of crystal growth of bilayer nickelates via different methods.

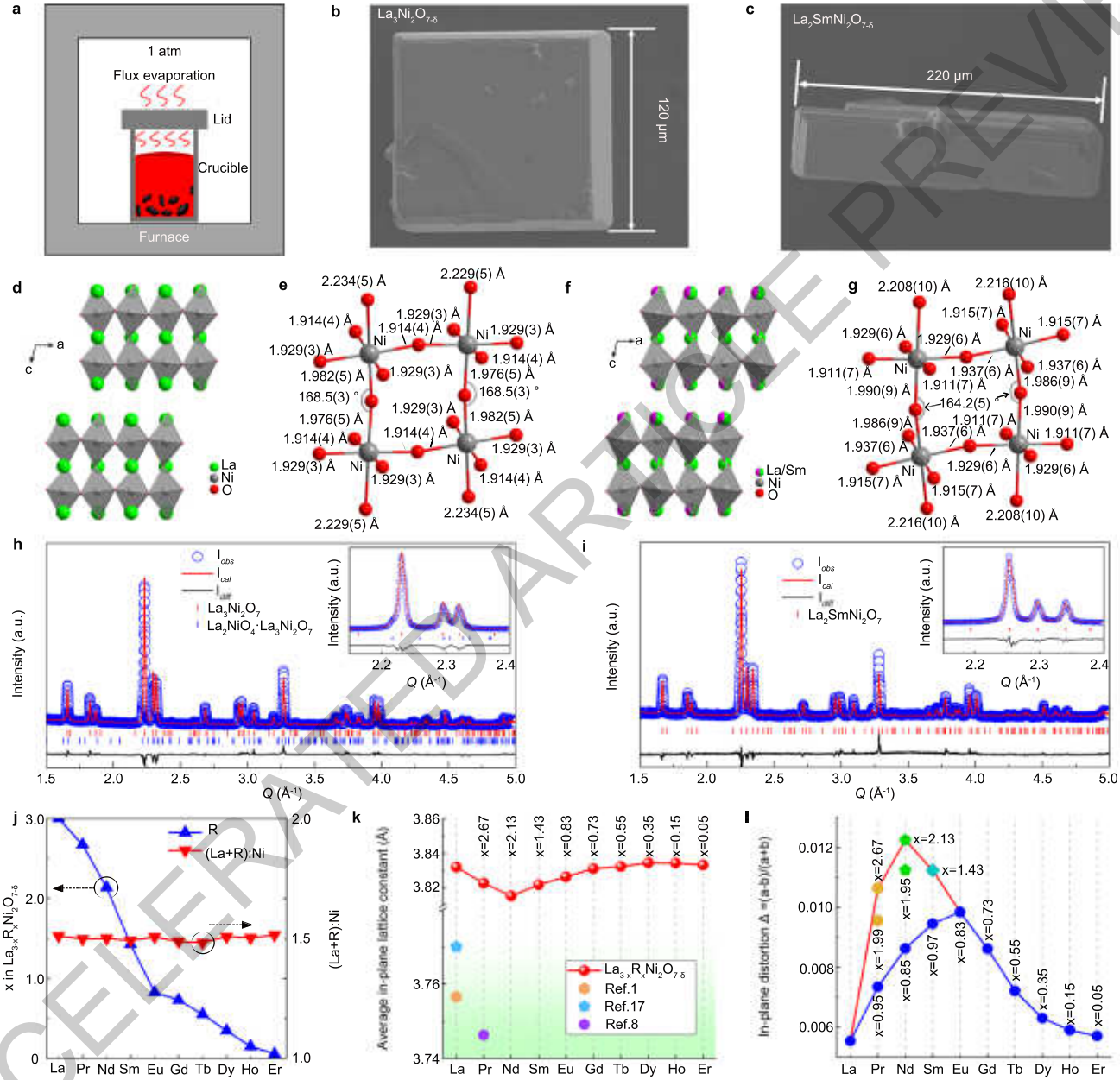

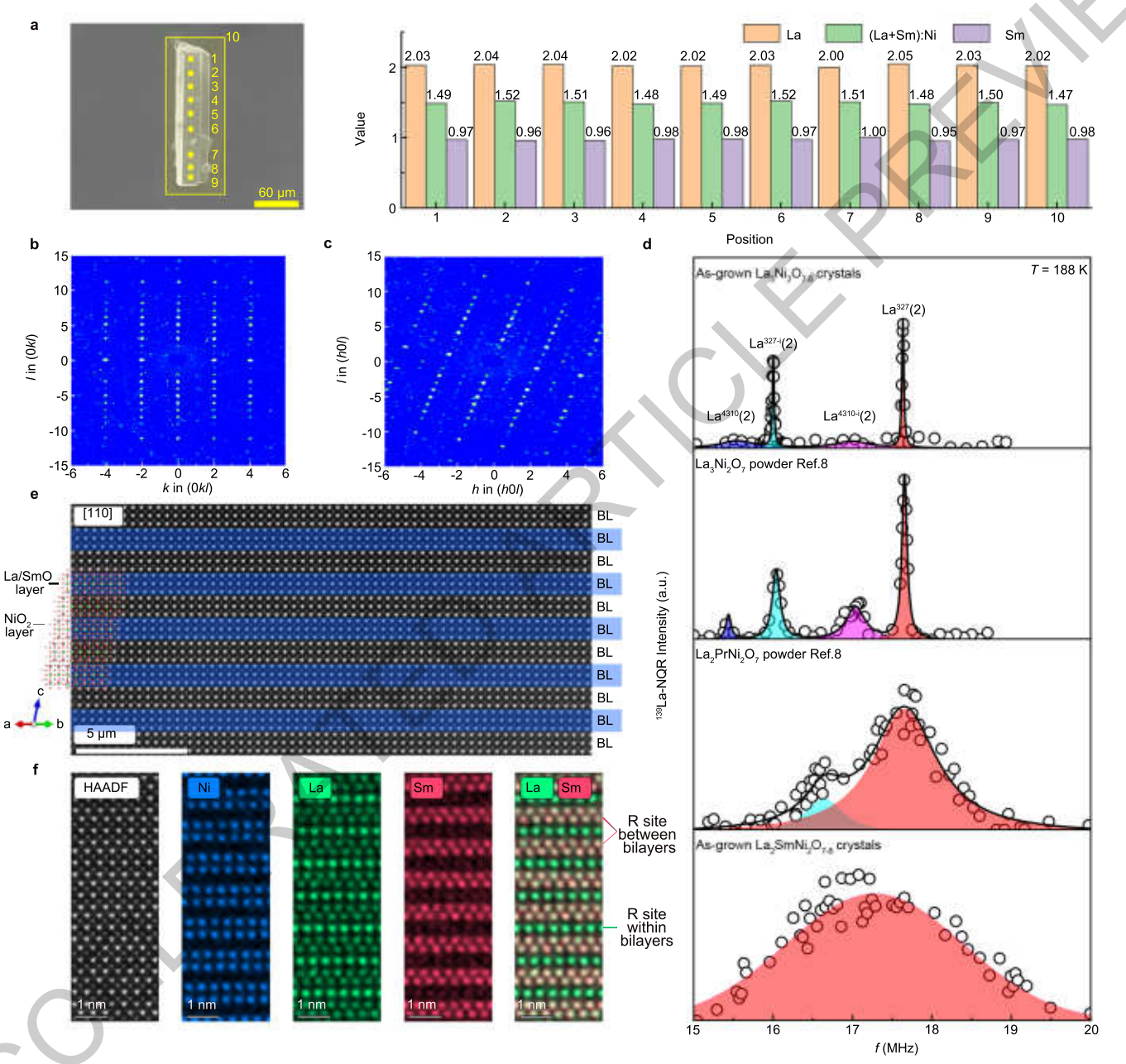

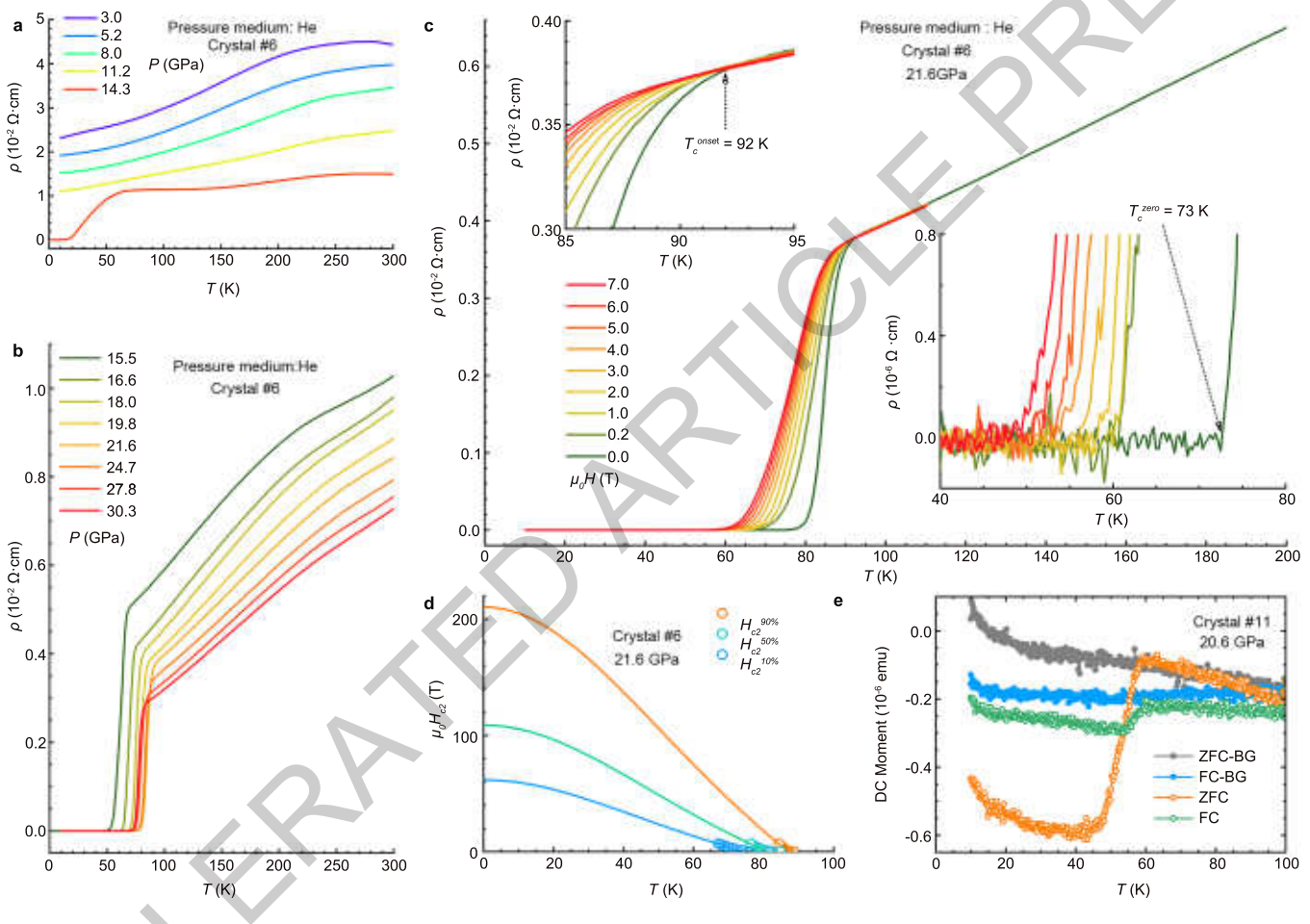

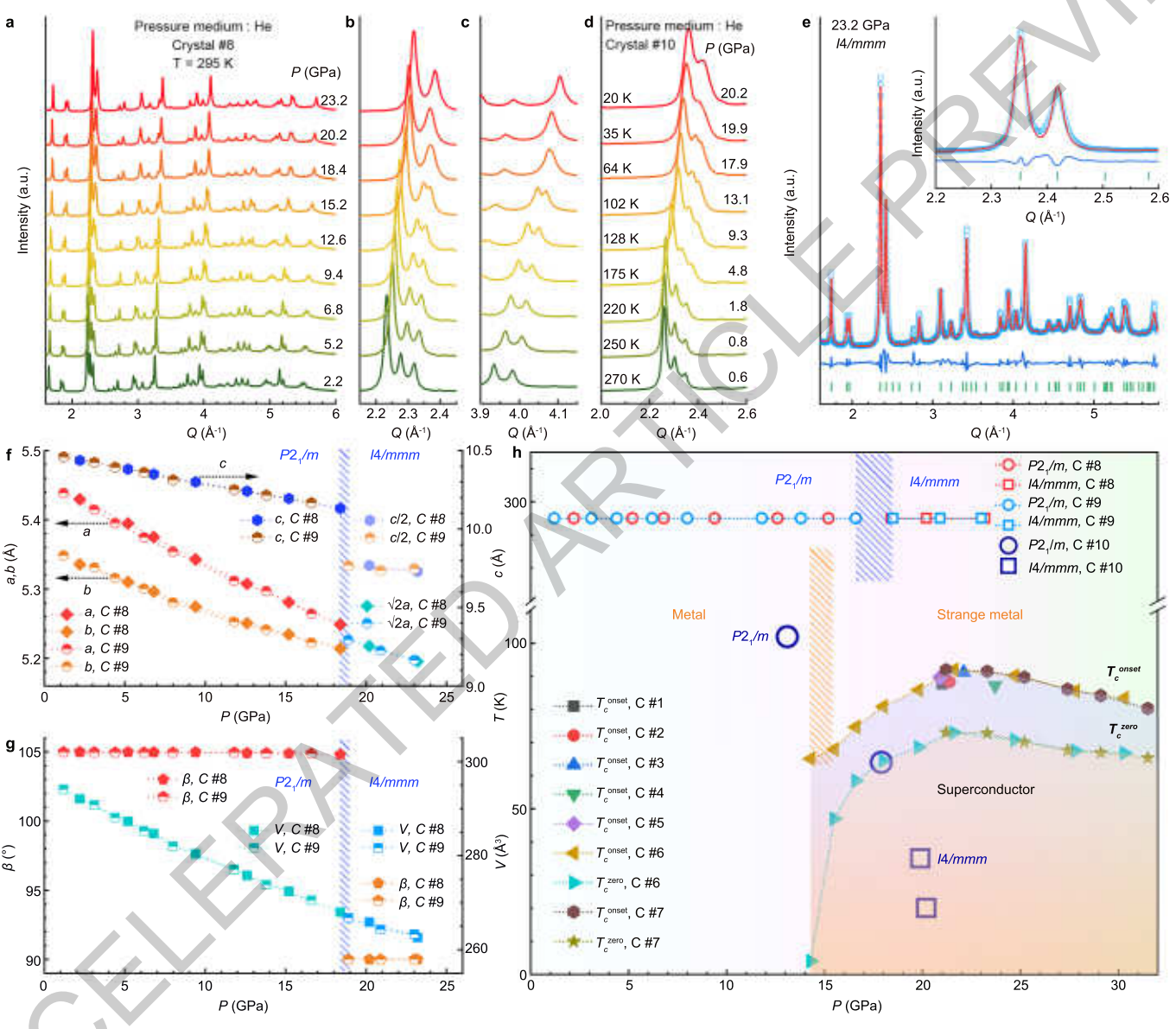

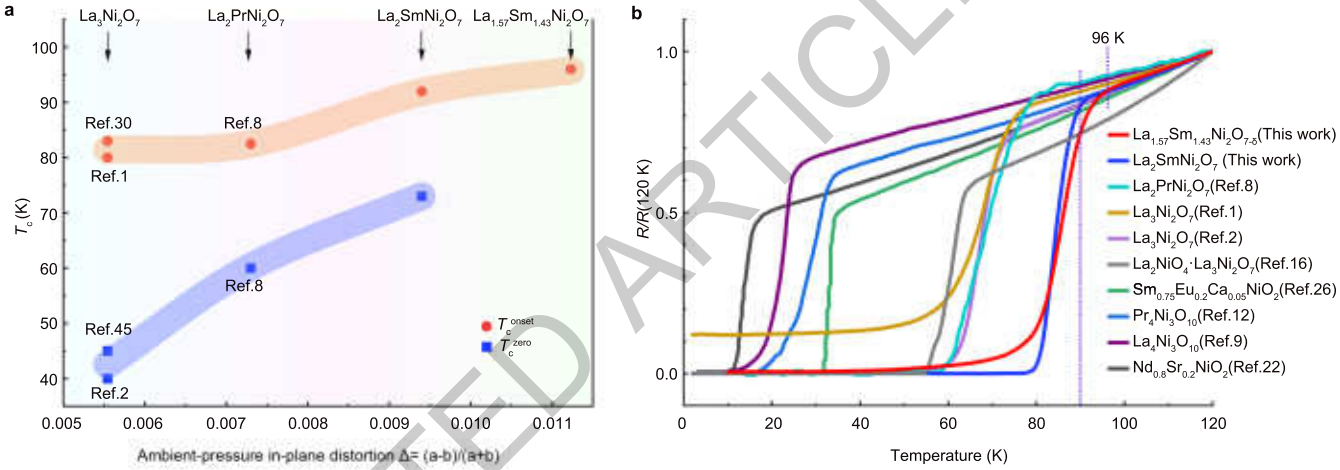
a
$La_3Ni_2O_7$
$La_2PrNi_2O_7$
$La_2SmNi_2O_7$
$La_{1.57}Sm_{1.43}Ni_2O_7$
Ref.30
Ref.8
Ref.1
Ref.8
Ref.45
Ref.2
T_c (K)
T_c^{onset}
T_c^{zero}
Ambient-pressure in-plane distortion Δ= (a-b)/(a+b)
b
96 K
R/R(120 K)
Temperature (K)
$La_{1.57}Sm_{1.43}Ni_2O_{7-\delta}$(This work)
$La_2SmNi_2O_7$ (This work)
$La_2PrNi_2O_7$(Ref.8)
$La_3Ni_2O_7$(Ref.1)
$La_3Ni_2O_7$(Ref.2)
$La_2NiO_4{\cdot}La_3Ni_2O_7$(Ref.16)
$Sm_{0.75}Eu_{0.2}Ca_{0.05}NiO_2$(Ref.26)
$Pr_4Ni_3O_{10}$(Ref.12)
$La_4Ni_3O_{10}$(Ref.9)
$Nd_{0.8}Sr_{0.2}NiO_2$(Ref.22)

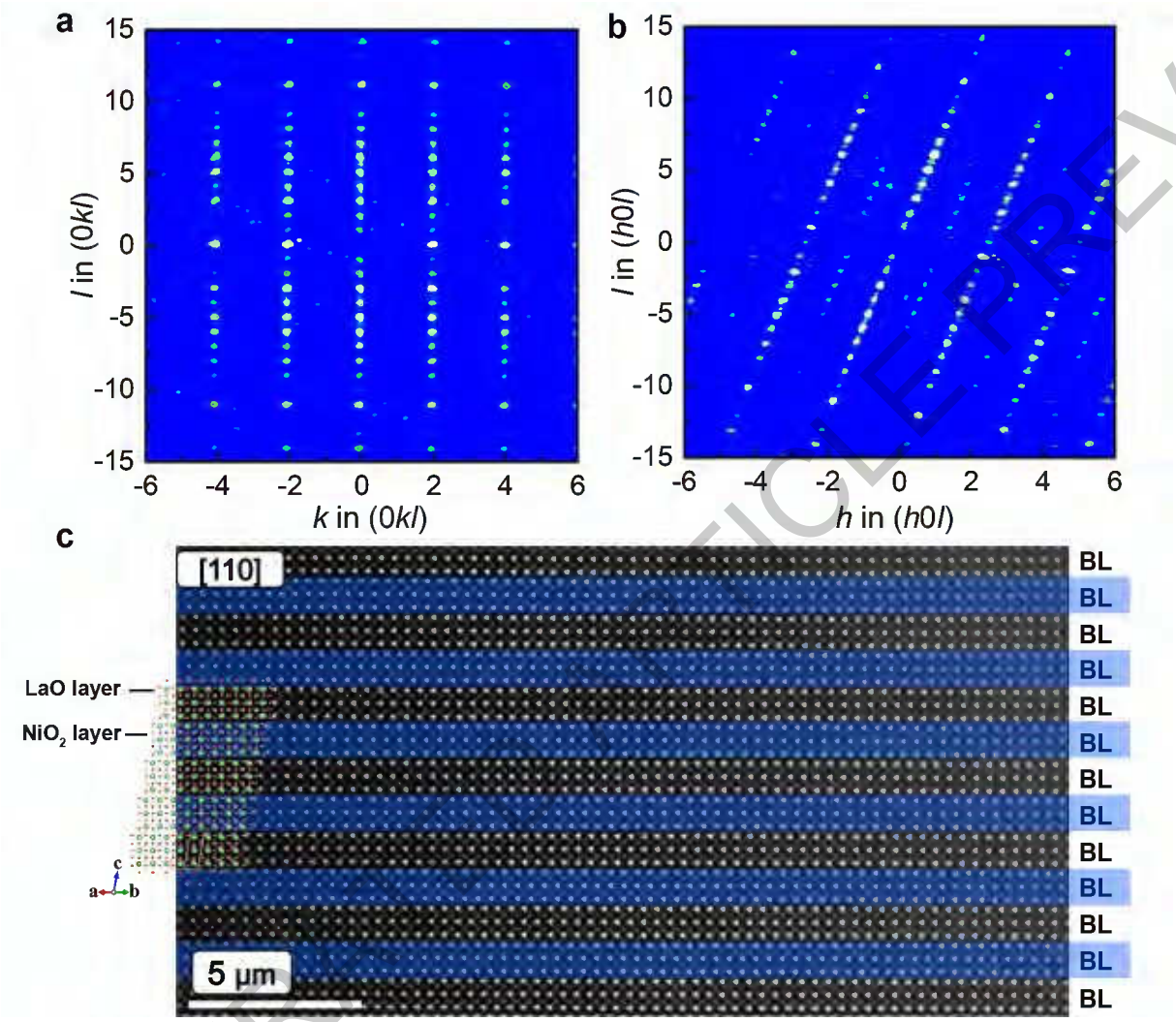

Extended Data Fig. 1

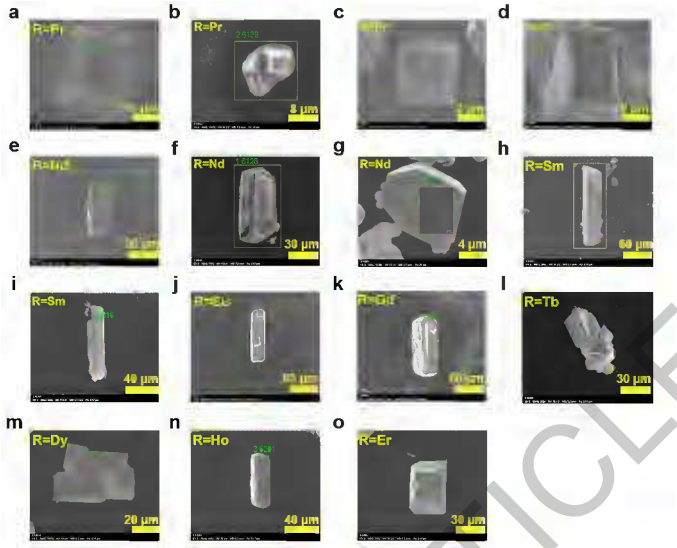

No.	R	La:R in flux (molar ratio)	La:R in as-grown crystals via EDS Measurement			No.	R	La:R in flux (molar ratio)	La:R in as-grown crystals via EDS Measurement		
			La	R	(La+R): Ni				La	R	(La+R): Ni
a	Pr	2:1	2.05	0.95	1.58	i	Sm	1:2	1.57	1.43	1.47
b		1:2	1.01	1.99	1.49	j	Eu	2:1	2.17	0.83	1.52
c		1:5	0.45	2.55	1.47	k	Gd		2.27	0.73	1.46
d		1:9	0.33	2.67	1.49	l	Tb		2.45	0.55	1.45
e	Nd	2:1	2.15	0.85	1.47	m	Dy		2.65	0.35	1.52
f		1:2	1.05	1.95	1.46	n	Ho		2.85	0.15	1.51
g		7:23	0.87	2.13	1.5	o	Er		2.95	0.05	1.54
h	Sm	2:1	2.03	0.97	1.49						

Extended Data Fig. 2

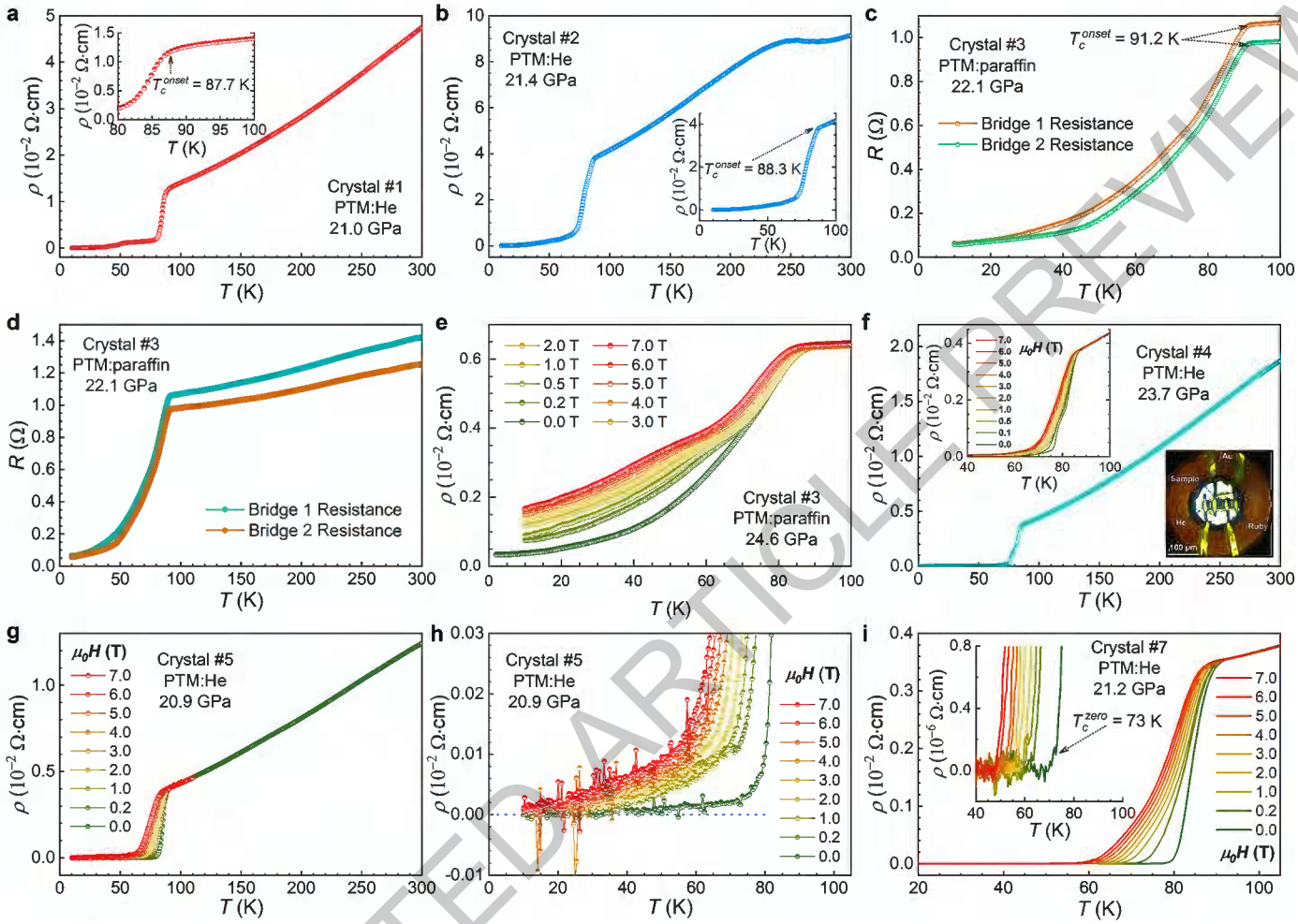

Extended Data Fig. 3

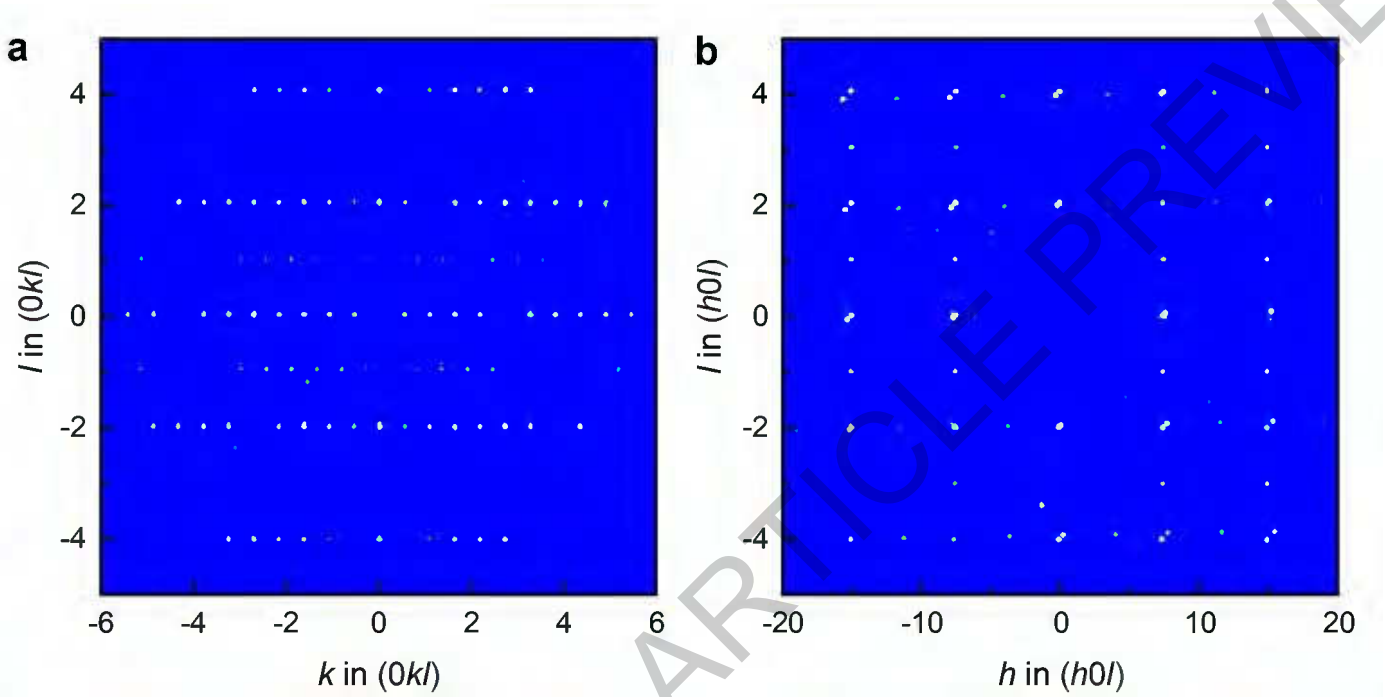

Extended Data Fig. 4

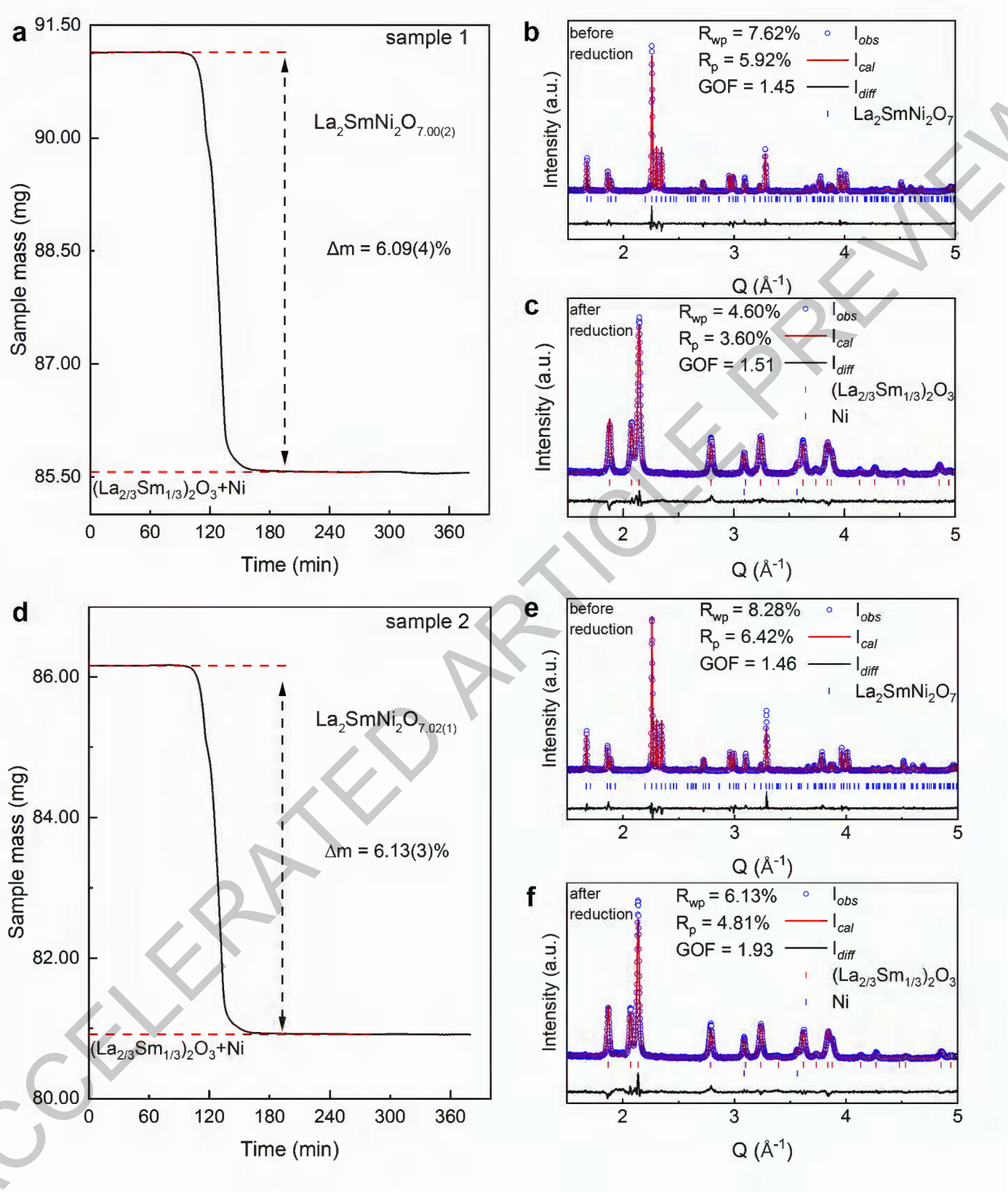

Extended Data Fig. 5

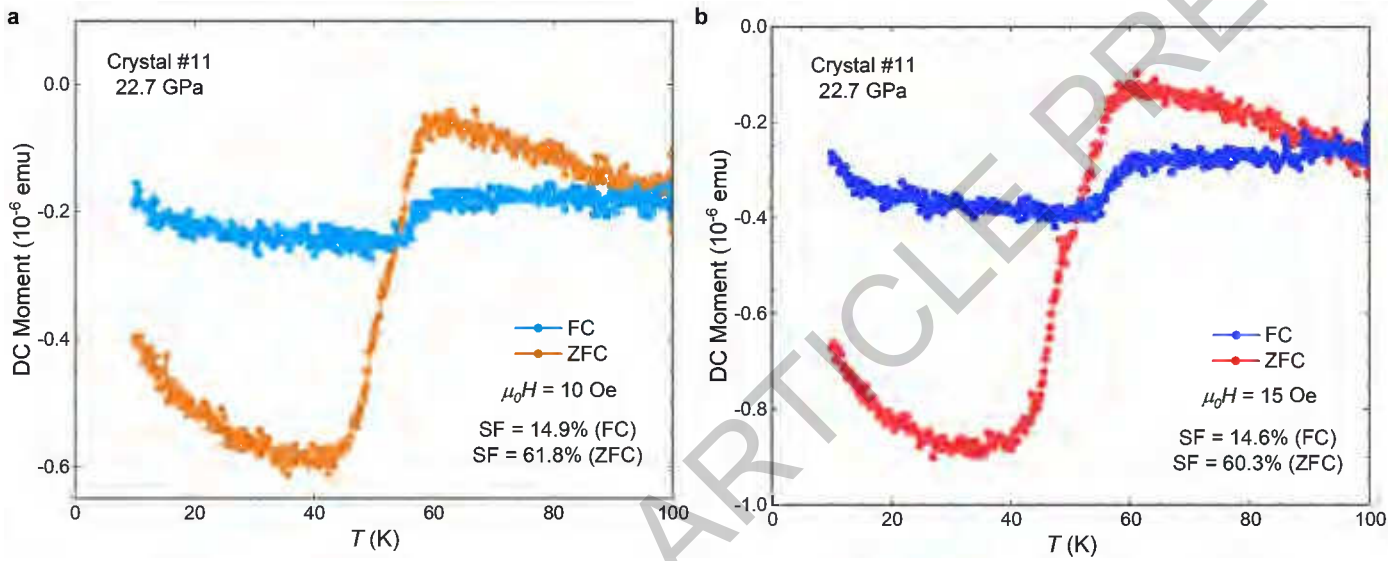

Extended Data Fig. 6

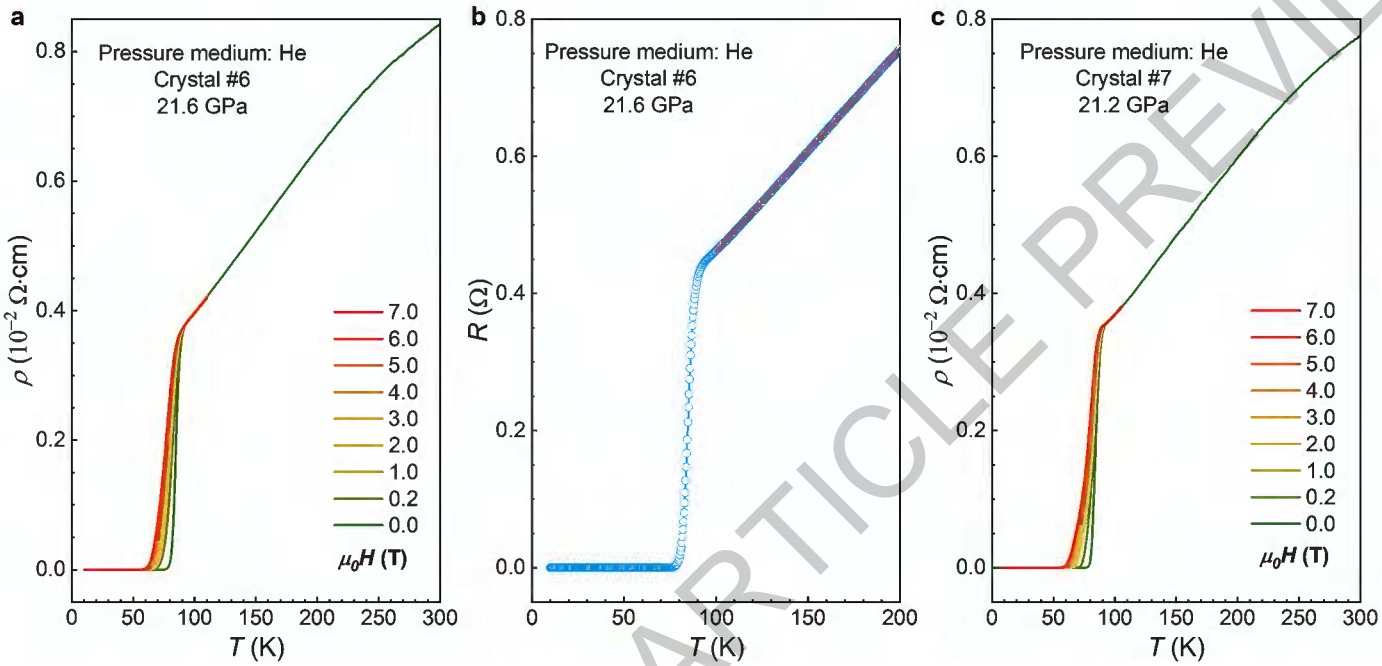

Extended Data Fig. 7

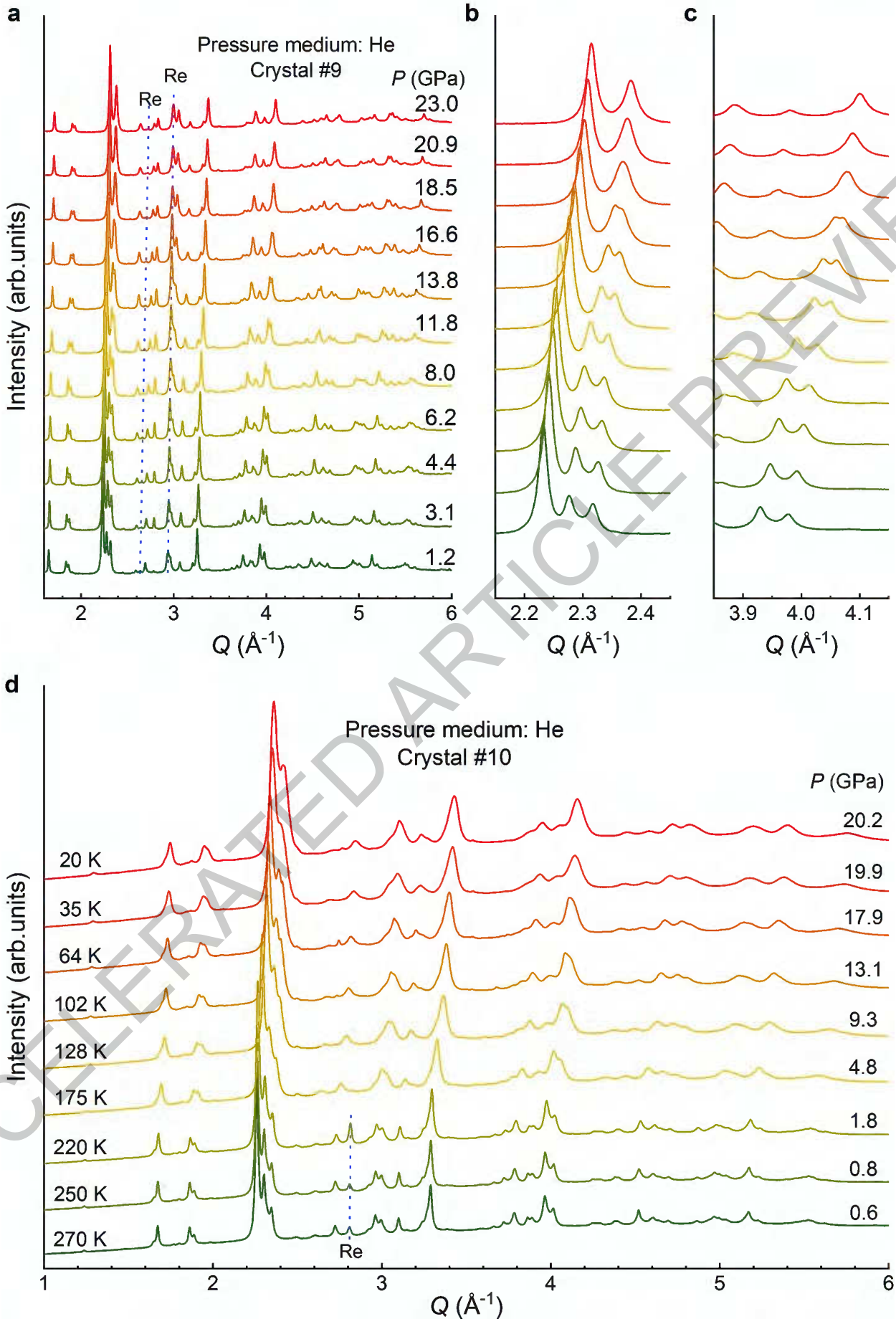

Extended Data Fig. 8

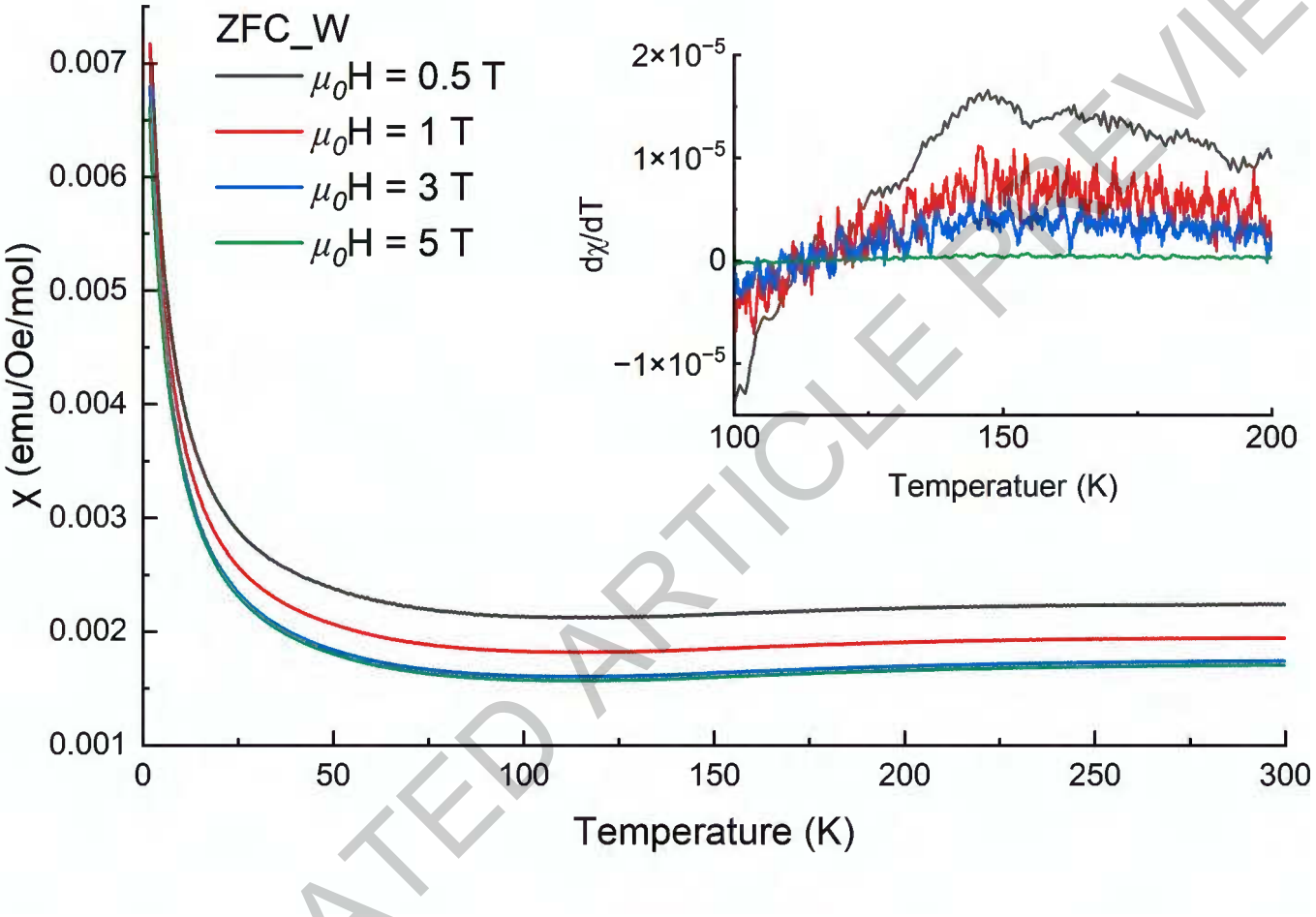

Extended Data Fig. 9

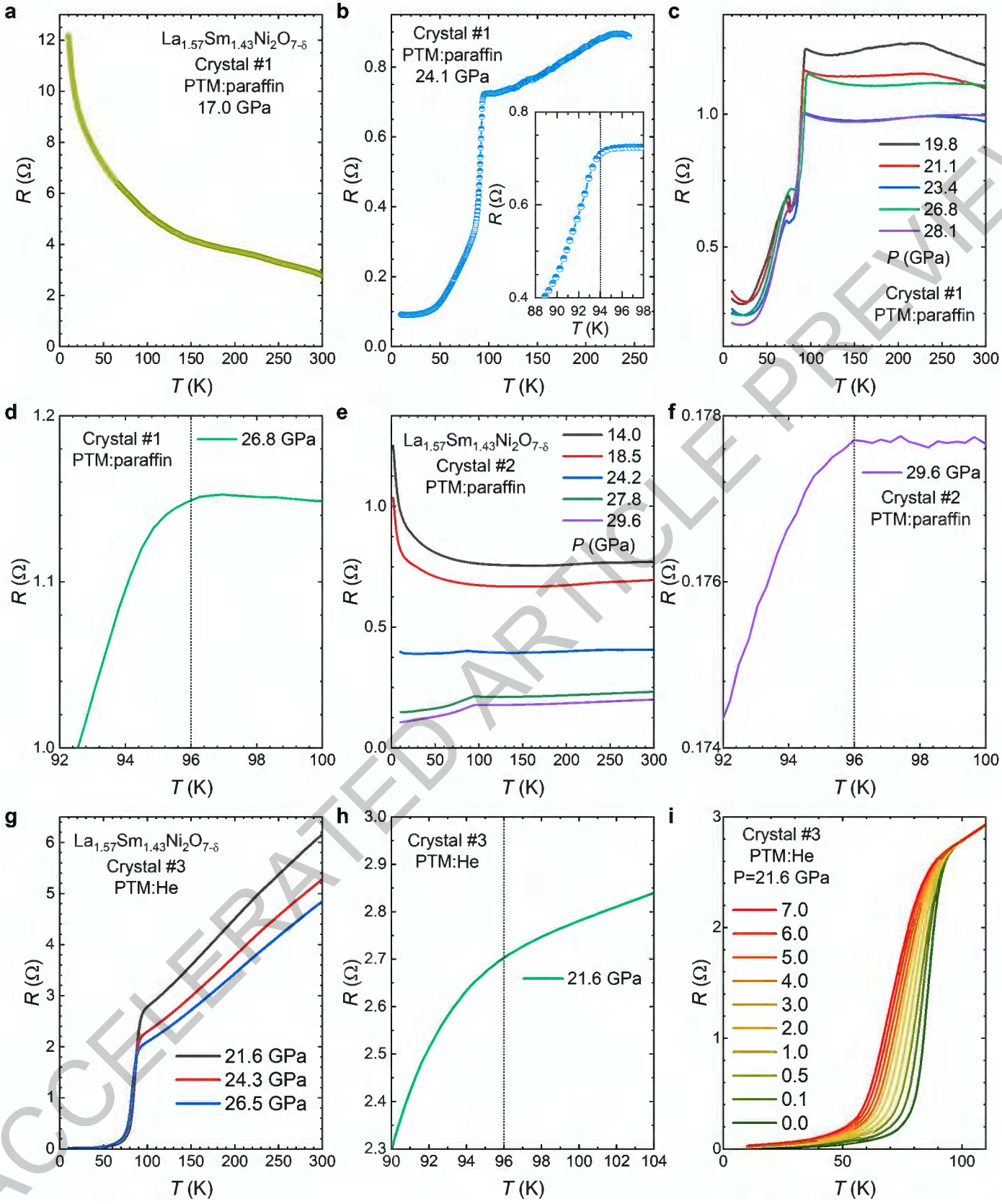

Extended Data Fig. 10

Extended Data Table 1 | Crystallographic data for $La_3Ni_2O_7$ and $La_2SmNi_2O_7$ from SXRD.

Empirical formula	$La_3Ni_2O_7$	$La_2SmNi_2O_7$
Formula weight	646.15	656.85
Temperature	296(2) K	296(2) K
Crystal system, Space group	Monoclinic, $P2_1/m$	Monoclinic, $P2_1/m$
Unit cell dimensions	a = 5.4370(2) Å b = 5.3978(2) Å c = 10.6173(4) Å β = 104.817(1)°	a = 5.4529(3) Å b = 5.3598(3) Å c = 10.4970(5) Å β = 105.053(2)°
volume	301.234(19) $Å^3$	296.26(3) $Å^3$
Z	2	2
Density(calculated)	7.124 g/cm^3	7.363 g/cm^3
Absorption coefficient	26.934 mm^{-1}	29.911 mm^{-1}
F (000)	566	575
Crystal size	0.055×0.041×0.035 mm^3	0.033×0.025×0.013 mm^3
Radiation	Mo K_α (λ = 0.71073 Å)	Mo K_α (λ = 0.71073 Å)
Θ range for data collection/°	1.984 to 33.132	2.009 to 31.527
Index range	$-8\le h\le 6$, $-8\le k\le -8$, $-16\le l\le 16$	$-8\le h\le 7$, $-7\le k\le -7$, $-15\le l\le 15$
Reflections collected	10929	12692
Independent reflections	1255 [R_{int}=4.36%, R_{sigma}=2.68%]	1078 [R_{int}=5.22%, R_{sigma}=2.21%]
Absorption correction	multi-scan	multi-scan
Refinement method	Full-matrix least-squares on F^2	Full-matrix least-squares on F^2
Data/ restrains/ parameters	1255 / 0 / 68	1078 / 0 / 70
Goodness-of-fit on F^2	1.13	1.13
Final R indicates [$I>2\sigma(I)$]	R_1=3.10%, wR_2=6.57%	R_1=3.71%, wR_2=8.61%
R indices (all data)	R_1=3.52%, wR_2=6.99%	R_1=4.83%, wR_2=10.04%
Largest diff. peak and hole	3.67 and -3.28 e. $Å^3$	4.44 and -3.78 e. $Å^3$

Extended Data Table 2 | Summary of crystal growth of bilayer nickelates via different methods.

Materials	Growth method	La:R (molar ratio)	T (°C)	Space group	Main advantage	Main issues/ comments	Ref.
$La_3Ni_2O_{7-\delta}$	Floating zone growth at 10-18 bar O_2	-	-	*Cmcm*	grow fast	High pO_2, narrow pO_2 range, competition of La_2NiO_4·$La_4Ni_3O_{10}$, intergrowth, expensive growth furnace	[1,38-40]
$La_3Ni_2O_{7-\delta}$	Flux growth at 0.2 bar O_2 using K_2CO_3 as a flux	-	1000 ~1050	$P2_1/m$	Ambient pressure, easy to access	Competition of hybrid R-P phases	This work
$La_{2.05}Pr_{0.95}Ni_2O_{7-\delta}$		2:1					
$La_{1.01}Pr_{1.99}Ni_2O_{7-\delta}$		1:2					
$La_{0.45}Pr_{2.55}Ni_2O_{7-\delta}$		1:5					
$La_{0.33}Pr_{2.67}Ni_2O_{7-\delta}$		1:9					
$La_{2.15}Nd_{0.85}Ni_2O_{7-\delta}$		2:1					
$La_{1.05}Nd_{1.95}Ni_2O_{7-\delta}$		1:2					
$La_{0.87}Nd_{2.13}Ni_2O_{7-\delta}$		7:23					
$La_{2.03}Sm_{0.97}Ni_2O_{7-\delta}$		2:1				Pure phase, large single crystals can be obtained	
$La_{1.57}Sm_{1.43}Ni_2O_{7-\delta}$		1:2				Competition of hybrid R-P phases	
$La_{2.17}Eu_{0.83}Ni_2O_{7-\delta}$		2:1					
$La_{2.27}Gd_{0.73}Ni_2O_{7-\delta}$							
$La_{2.45}Tb_{0.55}Ni_2O_{7-\delta}$							
$La_{2.65}Dy_{0.35}Ni_2O_{7-\delta}$							
$La_{2.85}Ho_{0.15}Ni_2O_{7-\delta}$							
$La_{2.95}Er_{0.05}Ni_2O_{7-\delta}$							